Lewy pathology in Parkinson's disease consists of a crowded organellar membranous medley

Authors: Sarah H. Shahmoradian[1,$], Christel Genoud[2], Alexandra Graff-Meyer[2], Jürgen Hench[3], Tim Moors[4], Gabriel Schweighauser[3], Jing Wang[1], Kenneth N. Goldie[1], Rosmarie Sütterlin[1], Daniel Castaño-Díez[1], Paula Pérez-Navarro[1], Evelien Huisman[4], Sabine Ipsen[3], Angela Ingrassia[4], Yvonne de Gier[4], Annemieke J.M. Rozemuller[5], Anne De Paepe[6], Johannes Erny[7], Andreas Staempfli[7], Joerg Hoernschemeyer[7], Frederik Großerüschkamp[8], Daniel Niedieker[8], Samir F. El-Mashtoly[8], Marialuisa Quadri[9], Wilfred F.J. van IJcken[10], Vincenzo Bonifati[9], Klaus Gerwert[8], Bernd Bohrmann[11], Stephan Frank[3], Markus Britschgi[11*], Henning Stahlberg[1*], Wilma D. J. van de Berg[4*], Matthias E. Lauer[6*]

Affiliations:

[1] Center for Cellular Imaging and NanoAnalytics (C-CINA), Biozentrum, University of Basel, Switzerland

[2] Friedrich Miescher Institute for Biomedical Research, Switzerland

[3] Division of Neuropathology, Institute of Pathology, University Hospital Basel, Switzerland.

[4] Department of Anatomy and Neurosciences, section Clinical Neuroanatomy, AO | 2M, Amsterdam Neuroscience, VU University Medical Center, Netherlands

[5] Department of Pathology, Amsterdam Neuroscience, VU University Medical Center, Netherlands

[6] Roche Pharma Research and Early Development, Chemical Biology, Roche Innovation Center Basel, Basel, Switzerland

[7] Roche Pharma Research and Early Development, Preclinical CMC, Roche Innovation Center Basel, Basel, Switzerland

[8] Department of Biophysics, Ruhr University Bochum, Germany

[9] Department of Clinical Genetics, Erasmus Medical Center, Rotterdam, Netherlands

[10] Center for Biomics, Erasmus Medical Center, Rotterdam, Netherlands

[11] Roche Pharma Research and Early Development, NORD DTA/Neuroscience Discovery, Roche Innovation Center Basel, Basel, Switzerland

[$] Current Address: Paul Scherrer Institute, Villigen, Switzerland

[*] Shared senior authors

Correspondence to: Matthias Lauer (matthias.lauer@roche.com), Wilma van de Berg (wdj.vandeberg@vumc.nl), Henning Stahlberg (henning.stahlberg@unibas.ch), and Markus Britschgi (markus.britschgi@roche.com)

Summary

Parkinson's disease, the most common age-related movement disorder, is a progressive neurodegenerative disease with unclear etiology. Key neuropathological hallmarks are Lewy bodies and Lewy neurites, which are neuronal inclusions that are immunopositive for the protein α-synuclein. In-depth ultrastructural analysis of Lewy pathology is key to understanding pathogenesis and progression of the disease. Using correlative light and electron microscopy on postmortem brain tissue of Parkinson's patients, we discovered a crowded membranous medley of vesicular structures, dysmorphic mitochondria and disrupted cytoskeletal elements in Lewy bodies and Lewy neurites, rather than the widely expected proteinacious filaments. The collapse and crowding of central organellar components was confirmed by stimulated emission-depletion microscopy, and chemical and optical imaging. A high lipid content was confirmed by lipidomics. The findings indicate ill-defined subcellular protein-lipid compartmentalization and point toward impaired organellar trafficking as a key driver of pathogenesis in Parkinson's disease.

Introduction

Lewy bodies (LB) are defined as roughly spherical eosinophilic intraneuronal proteinaceous inclusions, 5–25 µm in diameter. Soon after their microscopic discovery over 100 years ago, they became the main pathological hallmark of Parkinson's disease (PD) and Dementia with Lewy bodies (DLB). The protein α-synuclein (aSyn) is a major component of LB and considered to play a central role in their formation in both diseases[1]. The morphology of LB revealed by light microscopy (LM) varies depending on their location in the brain (brainstem, limbic or neocortical)[2, 3], may reflect maturation stage and genetic background, and their chemical composition is known to be complex[2, 4]. Lewy neurites (LN) are dystrophic neurites with the same immunohistochemical staining profile as LB, displaying prominent aSyn immunoreactivity[5, 6]. The morphology of LN also varies between brainstem and (sub)cortical brain regions[7].

The processes by which LB are formed and their role in neurodegeneration remain elusive. The current, leading hypothesis in PD research proposes that intraneuronal aSyn first accumulates as abnormal oligomers, possibly induced by extracellular pathogenic aSyn aggregates that were taken up and subsequently forms β-sheet rich amyloid fibrils, which are the basis of the LB[8]. Transmission electron microscopy (TEM) carried out on sarcosyl-insoluble fractions of brain tissue extracts or formalin-fixed, deparaffinized and resin-embedded brain tissue of patients with PD or DLB, revealed the ultrastructure of LB as filaments immunoreactive for aSyn[3, 9]. By contrast, evidence from ultrastructural studies on LB identified by neuroanatomical localization point to an electron-dense core and granular features[10]. Proteome studies have shown that LB contain more than 300 proteins, of which approximately 90 have been confirmed by immunohistochemistry in various postmortem studies and are associated with aSyn, protein degradation systems, molecular chaperones or axonal damage[2]. Thus, current literature about the nature of Lewy pathology is in several aspects still incomplete and lacks validation in order to make proper conclusions about pathogenesis and progression of Parkinson's disease. A clearer understanding of the building blocks of Lewy pathology is therefore urgently needed.

With the advent of modern technologies for electron microscopy such as energy filters, direct electron detectors, and drift-correcting software for tomography, we now have the possibility to obtain a clearer and more accurate picture of the 3D structure of such pathological inclusions, including the capability of distinguishing amyloid fibrils from lipid membranes. Here, we present an unprecedented 3D view of the structural components of LB and LN in well-preserved brain tissue from two sporadic PD patients using correlative light and electron microscopy (CLEM). The correlative methods employed clearly show that LB are comprised of aggregated membranous material rather than amyloid fibrillar structures, and that the aggregated membranes originate from vesicles and fragmented organelles, including mitochondria. Correlative multi-labeling and label-free compositional mapping methods were employed to corroborate these assignments in brain tissue of five PD patients, and demonstrated the presence and co-localization of aSyn, lipids, lysosomes and mitochondria in LB. The presence of lipids in LB was confirmed by mass spectrometry. The nanoscale information obtained suggests that the membrane aggregation observed in LB and LN is modulated by aSyn, and supports the hypothesis that impaired intracellular trafficking contributes to PD pathogenesis[11].

Results

A correlated light and electron microscopy (CLEM) approach was employed to identify LB/LN in advanced PD patients (Patients A-B, Table 1) who did not display any known PD genetic variants according to whole exome sequencing (WES) and analysis (Methods). By CLEM, we obtained a 3D view of the ultrastructure of two LB and one LN present in postmortem samples from the hippocampal CA2 (Patient A, Table 1) and *substantia nigra* (SN) (Patient B; Table 1), respectively. Before these experiments, the general presence and distribution of LB and LN in the SN and hippocampal CA2 were determined by light microscopy (LM) of paraffin-embedded tissue sections immunostained for aSyn (Fig. S1). CLEM was carried out on blocks prepared in parallel from the same tissue sample (herein referred to as parallel tissue blocks; Figs. S2-S4); aSyn immunoreactive inclusions were identified by histological staining and LM and 3D tomograms (Fig. 1) were recorded from adjacent tissue sections (i.e., regions immediately above or below in the block) by transmission electron microscopy (TEM). The use of CLEM in this way was crucial to distinguish LB from age-related changes, in particular *corpora amylacea* (*CA*); since LB and *CA* are of similar size and shape and can occur in close proximity in old individuals, they can be confused with one another in EM (Fig. S5). As described below, the TEM tomograms revealed mitochondria and numerous cellular organelles in LB (Fig. 1 and Movies 1-7). Densely compacted membranous structures and distorted vesicles were also visible; filaments were not detected.

In the overview tomograms, LB appear to be demarcated by a cellular membrane, with mitochondria clearly visible towards their periphery and in their interior (Fig. 1a-d). Besides abundant haphazard vesicular structures scattered throughout the LB, dense "dark" L-shaped structures resembling stacks of compacted membrane sheets with a membrane layer spacing of ~6 nm can also be distinguished (Fig. 1a-d, yellow arrowheads; Movie 4); herein referred to as tailed membrane stacks. They cannot be attributed to myelin, since the average membrane spacing of myelin sheaths is 10.7 nm in the central nervous system[12]. Furthermore, vesicular structures of varying electron density, some filled with more material than others (Fig. 1e-l), are observed within the LB. These are reminiscent of lysosomes and autophagosomes[13]. In addition, there are some features that appear to be distorted mitochondria (Figure 1i) and features (pink arrowhead) that clearly resemble the disk-like structures reported for aSyn-lipoprotein particles examined by cryo-EM[14]. Computational analysis of the vesicular structures (Fig. S6a) by sub-tomogram averaging revealed the 3D structure, indicating the presence of two basal planes as expected for membrane leaflets (Fig. S6b). As a control for the sub-tomogram averaging, neurofilaments present within a neurite from a healthy human brain (Fig. S6c) were similarly analyzed and shown to consist of a rod-like structure, as expected (Fig. S6d)[15]).

The same CLEM strategy (Fig. S2) was applied to precisely locate a LN and visualize its ultrastructure (Fig. S4; Patient B). This abnormal neurite contained disordered neurofilaments interspersed with vesicular structures reminiscent of mitochondria or remnants thereof (Fig. 2a, blue arrowheads), autophagosomes[13] (Fig. 2a, b, white asterisk), and a dense-core vesicle (Fig. 2a, black arrowhead; Movies 8-9). Importantly, a transition from order to disorder can be seen in the bottom part of the image shown in Fig. 2b; structures that look like neurofilaments[15] (Fig. 2b, white arrowheads) appear to become disrupted over the length of the neurite (Movies 8-9). Such disorganization was not observed in brain samples of aged non-neurological control subjects; the paths of neurofilaments are far more sharply delineated

(Fig. 2c, d), and mitochondria within the neurites exhibit intact cristae (Fig. 2d, black asterisk) (Movies 10-11).

To substantiate the ultrastructural assignments, 10 µm-thick cryostat sections collected from tissue blocks of the same SN region from the same patient (Patient B; Table 1) and the CA2 region of the hippocampus obtained from another late stage PD patient (Patient A; Table 1) were co-stained for lipids (Nile Red) and aSyn (immunohistochemistry labeling; Methods). Like Patient B, Patient A did not display any known genetic variants according to WES and PD gene analysis. In both cases, projections of the image stacks collected by confocal fluorescence microscopy showed co-localized staining of lipids and aSyn in the LB examined (Fig. S7), compatible with a high membrane content in LB.

Serial block-face scanning electron microscopy (SBFSEM)[16] was employed to investigate a larger tissue volume and characterize the LB. The 3D SBFSEM stacks collected document eight LB located in the SN of patient B (Fig. S8); one of these is presented in detail (Fig. 3) and 3D reconstructions are shown for another three (Movie 12). The 3D reconstructions reveal cytoplasmic inclusions of generally spherical, aggregated cellular material consistent in size with the aggregates visualized by optical microscopy of aSyn-immunostained LB in parallel tissue blocks (Fig. S1) and reported in the literature[1, 9]. The SBFSEM data also revealed the presence of many mitochondria (Fig. 3a-b, orange arrows) and other organelles resembling autophagosomes and lysosomes within the LB (Fig. 3a, b; aqua arrows), in agreement with Nixon et al.[13]. STED microscopy on separate sections taken from the same regions of the same patients confirmed that mitochondria closely cover the LB in a shell-like fashion (Fig. 3c-l; Movie 13).

Multiple labeling followed by 3D multi-color STED microscopy and 3D reconstruction, revealed widespread immunoreactivity for the lysosomal marker LAMP1 in LB within both hippocampal CA2 (Patient A) and SN (Patient B) tissue. Further, the mitochondrial marker Voltage-Dependent Anion Channel 1 (VDAC1) was localized towards the edge of LB and LN in both brain regions (Figs. 3, S9; Movie 13). The bright structures at the border of LB (Fig. 3d, i, n) might therefore represent a subset of mitochondria that are still intact or only mildly affected. The distribution motifs of pathologically modified aSyn (*e.g.*, phosphorylated at Serine 129, p-aSyn) immunoreactivity in hippocampal CA2 (Patient A) and SN (Patient B) are different; the latter indicates intense p-aSyn immunoreactivity at the border of the LB compared to the inner region (Fig. 3c, h, m), whereas the former indicates a more even distribution throughout the LB (Fig. S9a, f, k). Interestingly, the ring around LB in SN (Patient B) immunostained with p-aSyn (Serine 129) was surrounded by the mitochondrial marker VDAC1 (Fig. 3d, i, n). Overall, the data indicate that despite being different in the distribution of p-aSyn, both hippocampal and nigral LB and LN contain features derived from organelles, including mitochondria and lysosomes.

LB identified by SBFSEM were imaged at higher resolution by correlative TEM to define their ultrastructure more clearly. This involved periodically removing the sample blocks from the SBFSEM and cutting 50 nm-thick sections for the TEM analysis. From the higher resolution TEM images, LB are comprised of membrane fragments (Fig. 4). These have clearly distinguishable lipid bilayers and are similar in appearance to the membranes of organelles, such as mitochondria, and the plasma membranes of cells. One LB examined also exhibited dysmorphic, elongated mitochondria at its immediate periphery, either clustered with other membrane fragments and vesicles (Fig. 4b) or encased in distinct cellular compartments (Fig. 4c) in a state of what appeared to be partial degradation. Other mitochondria were more centrally located in the aggregate and surrounded by membrane fragments (Fig. 4d).

Clusters of membrane fragments, vesicles and structures resembling dysmorphic mitochondria (Fig. 4f), omegasomes (autophagosome precursors; Fig. 4f, g, black arrowheads) and lysosomes (Fig. 4f, g, pink arrowheads), were located towards the center of the LB. Yet, there was no indication of abnormal proteinacious filament structures. Note that other physiological filamentous structures were observed, e.g., cytoskeletal filaments were evident in regions within the same tissue section but distal to the LB (Fig. 4i, j). Furthermore, all mitochondria within the LB (Fig. 4b, c, d, f) were dysmorphic compared to mitochondria found within the cytoplasm of intact cells of the same tissue section, yet distal to the LB (Fig. 4e, i).

LB were examined by three additional methods to confirm the membranous lipid content shown by confocal fluorescence microscopy (Fig. 5), and thus corroborate the presence of the cellular or organellar membranes indicated by the EM data (Figs. 1, 3, 4). The first method combined coherent anti-Stokes Raman scattering (CARS)[17] with subsequent immunofluorescence staining and confocal laser scanning microscopy (CLSM) in correlative measurements, herein referred as correlative CARS-IF. CARS is a nonlinear optical imaging method that allows the label-free identification of the chemical composition of lipids and proteins in tissue at a resolution of 300 nm. Sections cut from frozen tissue blocks taken from the same brain regions of the patients used for the EM and LM studies were investigated, namely the CA2 region of Patient A, and the SN region of Patient B. CARS detected high lipid content in the center of aSyn-labeled LB. Furthermore, lipids and aSyn were inhomogeneously distributed within the LB, and the intensity distribution profiles of the two signals were similar: areas that gave a higher aSyn signal also gave a higher lipid signal (Fig. 5a-d).

The second method used to confirm the presence of lipids, combined high-definition Fourier transform infrared (FTIR) spectroscopic imaging with subsequent correlative immunofluorescence staining and confocal laser scanning microscopy (CLSM), herein referred as correlative FTIR-IF. FTIR imaging exploits the fact that the mid-infrared region absorbed by chemical bonds (*e.g.,* C=O, C-H, N-H) is related to their chemical environment, *i.e.,* to the presence and composition of specific biomolecules within cells or tissue (*i.e.*, lipids, protein, DNA)[18], and does not require the use of labels. IF was used to detect aSyn. The FTIR-IF results confirmed that LB are rich in aSyn and lipids (Fig. 5E-H).

Finally, liquid chromatography-mass spectrometry (LC-MS) and lipidomics analyses were applied to LB isolated by laser-capture microdissection microscopy (LCM). LB identified by aSyn-immunostaining were extracted from 7 µm-thick cryostat-cut tissue sections of SN (~3050 LB) and CA2 (~2700 LB) of the same PD patients (Patients B and A, respectively; Table 1) using LCM. The subsequent analysis confirmed the high cell membrane related lipid content indicated by other methods, with the mass spectra showing strong peaks corresponding to sphingomyelin and phosphatidylcholine for LB isolated from both the SN and hippocampal CA2 sector (Fig. S10). Similar peaks were observed in myelin-rich, and hence lipid-rich, regions dissected from the corpus callosum of a non-demented control patient.

Together, these three orthogonal methods confirm that LB contain both aSyn and lipids in close proximity and show that they are rich in lipids found in other physiological and lipid-rich structures in the brain, e.g. organellar membranes. They fully corroborate the interpretation of the microscopy data, confirming that LBs contain aSyn, lipids, lysosomes and mitochondria.

Discussion

The results of advanced electron and optical imaging techniques show that aSyn-labelled LB and LN in brain tissue of PD patients consist of a crowded medley of mitochondria, lysosomes and vesicles. This is the first time that evidence is provided for the building blocks of LB and LN in human brain tissue at nanometer scale. Our results support a key role for damaged organelles in the formation of LB and LNs, a major process in the pathogenesis of PD.

Here, SN and hippocampal CA2 regions dissected from the brains of clinically diagnosed and pathologically confirmed PD patients were examined by a range of complementary correlative methods to study Lewy pathology at the nanometer scale in 3D and learn more about the ultrastructure and composition of LB and LN. No known PD genetic variants were found by WEST for the patients. Correlative LM on consecutive alternating ultra-thin sections of brain tissue immunolabeled for aSyn confirmed that cellular organelles and membranes observed by TEM microscopy (Figs. S3, S4) and tomography, indeed constituted *bona fide* Lewy pathology (Figs. 1a-d, 2; Movies 1-9). SBFSEM of corresponding tissue from the same patient, stained with heavy metals to enhance contrast, provided 3D reconstructions of Lewy pathology across volumes spanning tens of microns (Fig. 3, Movie 12), rather than the 100-200 nm typically accessible by TEM, giving a comprehensive 3D view of LB and LN in tissue at a spatial resolution of ~16 nm. Comparatively smaller sub-regions of interest containing LB were investigated at higher resolution and in 3D by TEM tomography (Fig. 1e-l). Together, this led to the discovery of ultrastructural membranous features in LB and LN; contrary to expectations, we did not detect filaments in the explored Lewy pathology. The EM was complemented by confocal IF microscopy, 3D reconstruction of multi-labeling STED microscopy data, correlative CARS-IF and FTIR-IF imaging. These methods showed that aSyn, lipids and markers for lysosomes and mitochondria are present in LB and LN and provided information about their distribution. As visualised by SBFSEM, mitochondria concentrate towards the edge of LB forming a type of shell around them (Fig. 3a, b), as corroborated by STED (Fig. 3f, k, p). The presence of membrane lipids, in particular sphingomyelin and phosphatidylcholine, in LB was verified further by LC-MS analysis of laser-capture micro-dissected LB (Fig. S10).

While previous studies also indicated lipid content in LB[19], the discovery of a crowded medley of membrane fragments, mitochondria, vesicular structures, including some that resemble lysosomes and autophagosomes, intermingled with non-fibrillar aSyn in LB and LN, provokes new theories about the mechanisms contributing to the formation of Lewy pathology in PD. The data support existing hypotheses regarding the role of mitochondrial and lysosomal dysfunction as pathogenic mechanisms in PD. For instance, mutations in certain genes (e.g. *SNCA, PARK2, PINK1, DJ-1*) have been linked to familial recessive or autosomal dominant forms of PD, and possible biological processes mediated by these genes are associated with mitochondrial function[20, 21]. Although difficult to corroborate, a role for these genes in idiopathic PD (except for *SNCA*)[22], the presence of mitochondria around (Figs. 1, 3, 4) and within LB (Fig. 3, 4, S9) indicates a potential mitochondrial instability or dysfunction in certain neurons in PD. Many of the Mendelian genes (*SNCA, LRRK2, VPS35)*, *GBA* (the single risk gene for PD), and various risk *loci* are associated with autophagy and lysosomal degradation[20, 21]. For example, certain mutations in *GBA* lead to ER stress and autophagic perturbations, as observed in iPSC-derived dopaminergic neurons of PD patients carrying a GBA mutation[23]. Mitophagy is a specialized form of organellar autophagy targeting damaged mitochondria in a mechanism regulated by PARK2 and PINK1[24].

Mitochondrial homeostasis is known to be influenced by aSyn, which interacts with mitochondria-associated ER membranes, and is suggested to play a role in disrupting autophagy, endosomal transport, and ER traffic to the Golgi[25]. The fact that mitochondria co-localize with membrane fragments and membranous features reminiscent of autophagosomes within Lewy pathology (Figs. 3, 4), supports the hypothesis that dysregulation of intracellular degradation pathways for proteins and entire organelles is a determining factor in PD.

The correlative TEM tomograms acquired show clearly that, like LB, LN are also primarily composed of membrane fragments, dysmorphic mitochondria and structures reminiscent of lysosomes and autophagosomes, as well as ill-defined cytoskeletal building blocks (Fig. 2a, B). To the best of our knowledge, such an observation has not been reported before. The cytoskeletal abnormalities recorded by CLEM in two regions of a LN (Figs. 2a, b; S4g, red dotted boxes) support the idea that neurofilaments become disrupted, possibly through proximally experiencing an increase of oxidative stress[26, 27]. The 3D STED data also showed that LN contain many mitochondria and lysosomes. Taken together, a crowded medley of damaged organelles and proteins would be sufficient to disrupt axonal trafficking. Indeed, recent large-scale proteome studies have linked LRRK2 and PINK1, which are associated with PD, to the Rab family of small GTPases, which regulate intracellular membrane trafficking[20, 21, 28].

Unexpectedly, although the local concentration of aSyn was high within LB and LN, a specific aggregated form (*e.g*., fibrils) was not observed. Rather, the data indicate that aSyn may modulate the compartmentalization and function of membranes and organelles, within the medley of dysmorphic features. This prompts an alternative hypothesis about the role of aSyn in the formation of Lewy pathology in PD (Fig. 6). Notably, the physiological role of aSyn in the presynaptic terminal includes remodeling of membrane, clustering of synaptic vesicles and maintaining synaptic vesicle pools, promoting SNARE-complex assembly, and modulating the release cycle of synaptic vesicles[29]. The formation of structures called 'nanodiscs' by aSyn and lipids *in vitro* has also been demonstrated[30], and it is tempting to suggest that these are a rudimentary form of the membrane 'discs' observed in LB, one of which is clearly shown in Fig. 1I (pink arrowhead). Furthermore, the observation of tailed membrane stacks exhibiting a bilayer separation of ~6 nm (Fig. 1a-d, yellow arrowheads; Movie 4), different than expected for myelin, may point to another role of aSyn in modulating membrane interactions. Intriguingly, certain N-terminal mutations that cause reduced solubility of aSyn *in vitro* lead to the formation of round inclusion-bodies in transfected primary rat neurons[31], but whether membranes or organelles play a role in this model needs to be demonstrated.

In future experiments, it will be interesting to explore how aSyn influences the formation of Lewy pathology in concert with vesicles and cytoplasmic organelles. Whether the development of Lewy pathology is linked to a putative liquid demixing of intrinsically disordered proteins, such as aSyn[32], also needs to be further investigated. Further, it will be important to consider the apparent co-localization of mitochondrial markers and what is considered to be pathologically modified aSyn (*e.g.*, p-aSyn) in the outer shell of LB in the SN (Fig. 3f, k, p), a region of high oxidative stress[26, 27]. In light of the presented findings, it will be interesting to explore whether the animal and cellular models of intracellular aSyn accumulation reveal similarities to our observation in human brain, thereby leading to more representative translational models of PD and related synucleinopathies.

In summary, based on our observations at the nanoscale in highly relevant human brain samples from PD patients, we present here a new theoretical model, in which not amyloid aSyn fibrils but lipid membrane fragments and distorted organelles together with aSyn are the

main building blocks for the formation of LB and LN (Fig. 6). These results have major implications for the understanding of the pathogenesis of PD, and could lead to new approaches for models and biomarkers and point to novel drug targets for this and related diseases.

Methods

Human Postmortem Brain Tissue Samples

Post-mortem tissue samples from two donors (Patients A and B) with clinical diagnosis PD with dementia (PDD) and one non-demented control (Patient C), all with ~5 hrs post-mortem delay, were obtained from the Netherlands Brain Bank (NBB, www.brainbank.nl; Table 1) and the Normal Aging Brain Collection (Dept. Anatomy and Neurosciences, VUmc), respectively. Tissues were collected using a rapid autopsy protocol (NBB). All donors had given written informed consent for a brain autopsy and the use of the material and clinical information for research purposes. Detailed neuropathological and clinical information was made available, in compliance with local ethical and legal guidelines, and all protocols were approved by the local institutional review board.

At autopsy, four 0.5cm-thick adjacent brain slices of the mesencephalon and hippocampus (mid) were collected. Cubes of ~1-2 mm^3 of the ventral part of the *substantia nigra pars compacta* (SNpc) and hippocampal CA2 regions were dissected and fixed for 6 hours in a mixture of 2% paraformaldehyde/2.5% glutaraldehyde in 0.15 M cacodylate buffer with 2 mM calcium chloride, pH 7.4 and then washed with PBS. One slice of mesencephalon and hippocampus was directly snap-frozen for processing for LCM and subsequent lipidomics and CARS analysis.

The PD patients fulfilled the United Kingdom Parkinson's Disease Society Brain Bank (UK-PDSBB) clinical diagnostic criteria for PD[33]. Neuropathological evaluation was performed on 7 µm formalin-fixed paraffin-embedded sections collected from multiple brain regions according to the guidelines of BrainNet Europe. As is routine for such patients, staging of Alzheimer's disease was evaluated according to the Braak criteria for NFTs[34], CERAD criteria adjusted for age and Thal criteria[35]. The presence and topographical distribution of aSyn (monoclonal mouse anti-human-α-synuclein, clone KM51, Monosan; Fig. S1) was rated according to Braak's staging scheme for aSyn[7] and a modified version of McKeith's staging system for aSyn (*i.e.*, brainstem, limbic system, amygdala-predominant or neocortical[36].

Whole Exome Sequencing and PD Gene Analysis

Postmortem brain tissue from Patients A and B were analyzed by WES with a focus on the analysis of the PARK genes and additionally some genetic risk factors for dementia. No known genetic variants were detected. Variants were to be reported if they fulfilled the following four criteria: (1) Variant(s) located within the following list of genes associated with PD or Parkinsonian syndromes: ATP13A2; ATP6AP2; CHCHD2; DNAJC13; DNAJC6; EIF4G1; FBXO7; GBA; LRRK2; PARK2; PARK7; PINK1; PLA2G6; RAB39B; SNCA; SYNJ1; TARDBP; VPS35; VPS13C; MAPT; GRN; TMEM230; POLG; DCTN1; PTRHD1. (2) Possible splicing variants → intronic or exonic variants (synonymous variants have been included) located within 10 bp at the exon-intron boundaries. (3) Exonic variants that have a coding effect (synonymous variants have been excluded). (4) Novel variants or variants present with a minor allele frequency (MAF; below 1%) in the following publicly available databases: NHLBI Grand Opportunity Exome Sequencing Project (ESP) (http://evs.gs.washington.edu/EVS/); Exome Aggregation Consortium Browser (ExAC) (http://exac.broadinstitute.org/); 1000 Genomes

(http://browser.1000genomes.org/index.html); dbSNPs (https://www.ncbi.nlm.nih.gov/projects/SNP/); Genome of the Netherlands (GoNL) (http://www.nlgenome.nl/).

Correlative Light and Electron Microscopy

The CLEM workflow is summarized in Fig. S2. Fixed postmortem human brain tissue (2% filtered paraformaldehyde/2.5% glutaraldehyde in 0.15 M cacodylate buffer with 2 mM calcium chloride, pH 7.4) was washed in cacodylate buffer and kept at 4 ºC for 1-2 days. Tissue sections were then collected at 40-60 µm on a vibratome and washed in cold cacodylate buffer, post-fixed in potassium ferrocyanide in cacodylate buffer with osmium tetroxide, washed with double-distilled water, and immersed in filtered thiocarbohydrazide solution. After this second wash step, sections were post-fixed in osmium tetroxide, rinsed again and stained with uranyl acetate at 4 ºC overnight. The following day, sections were rinsed, stained with lead aspartate solution at 60 ºC, dehydrated in a graded alcohol series on ice, and embedded in Durcupan resin. After resin hardening, small pieces of the resin-embedded tissue (~ 1 mm x 1 mm) were cut and mounted on standard aluminum pins, then physically cut using a razor blade into a trapezoid shape, which is optimal for the collection of serial tissue sections.

All tissues sections were generated using a physical ultramicrotome (Ultracut EM UC7; Leica Microsystems, Germany) and cut at a thickness of 100-200 nm. They were alternately collected on Superfrost™ Plus glass slides (Thermo Fisher Scientific, USA) for later light microscopy (LM) and EM grids (EMS Diasum, PA, USA) with a carbon-stabilized formvar film for TEM imaging. Slides were processed for DAB immunohistochemistry using mouse anti-aSyn (Invitrogen 180215, LB509 concentrate) diluted 1:70, with a pre-treatment of concentrated formic acid for 5 minutes followed by immersion in PBS and 60 minute microwave irradiation at 90 ºC.

The slides were screened by LM and compared side-by-side to identify LB and LN. LM images of selected slides displaying LB/LN were collected at 40x magnification using a Zeiss Axiophot (Carl Zeiss Microscopy) with monochromatic light, and the 40x individual black and white images were manually stitched together using Adobe Photoshop CS6 (Adobe Systems Incorporated) to create a montage revealing the trapezoid shape of an individual tissue section. The full montage representing the individual tissue section was then cropped to the limits of the tissue borders using an edge-detection lasso tool, which followed the trapezoid shape of the tissue sections. TEM images of EM grids that contained tissue sections immediately adjacent to those on the selected LM slides, were collected either on a Talos 200 keV TEM (FEI, Thermo Fisher, USA) and manually stitched together using Adobe Photoshop, or on a Titan Krios 300 keV TEM (FEI, Thermo Fisher, USA) using the SerialEM[37] montage option. The resulting EM montage was overlaid with the corresponding LM montage obtained for the alternating tissue sections collected on a glass slide, to define the specific location of the LB/LN in the TEM images (Fig. S3b, S4c) and guide the collection of subsequent higher resolution images and electron tomography. The collection of serial tissue sections on a single EM grid meant that the same LB or LN was present multiple times and that obstruction of the LB or LN by a grid bar was not an issue, since another section of the same grid, where it was not obscured, could be used (Fig. S4a).

For TEM tomography, samples were imaged at cryogenic temperatures using a Titan Krios (FEI, Thermo Fisher Scientific, USA) equipped with a Quantum-LS energy filter (20 eV slit width) and a K2 Summit Direct Electron Detector (Gatan, Pleasanton, CA, USA) and operated at 300 kV acceleration voltage. Tilt series were recorded using the SerialEM software[37] and a "dose-symmetric Hagen tilt-scheme". The latter procedure begins at low tilt

and then alternates between increasingly positive and negative tilts to maximize the amount of high-resolution information maintained in the tomogram for subsequent subtomogram averaging and 3D color segmentation, and also yields improved tracking between sequential tilt angles[38]. Images for the tilt series were collected at 3° increments over a range from -60° to 60° at a nominal defocus within 5µm. The final pixel size was 0.54 nm at the specimen level.

Tilt series alignment by cross-correlation and patch-tracking followed by 3D reconstruction of unbinned tomograms were performed using *etomo* of the IMOD software[39]. Resulting tomograms were reduced by a factor of 4 in all dimensions. Semi-automatic 3D color segmentation of the tomograms was performed by user-interactive thresholding and volume rendering using the Amira 6.0 software (FEI). Movies were constructed using Amira 6.0. Sub-tomographic texture analysis was performed using the *Dynamo* software[40].

Serial Block-Face Scanning Electron Microscopy and Correlative Transmission Electron Microscopy

Fixed postmortem human brain tissue (2% filtered paraformaldehyde / 2.5% glutaraldehyde in 0.15 M cacodylate buffer with 2 mM calcium chloride, pH 7.4) was washed in cacodylate buffer and kept at 4 ºC for 1-2 days. Tissue sections were then collected at 40-60 µm on a vibratome, washed in cold cacodylate buffer, post-fixed in potassium ferrocyanide in cacodylate buffer with osmium tetroxide, washed with double-distilled water, and immersed in filtered thiocarbohydrazide solution. After this step, sections were post-fixed in osmium tetroxide, rinsed again and stained with uranyl acetate at 4 ºC overnight. The following day, sections were rinsed, stained with lead aspartate solution at 60 ºC, dehydrated in a graded alcohol series on ice, and embedded in Durcupan resin. After resin hardening, small pieces of the resin-embedded tissue (~ 1 mm x 1 mm) were cut and mounted on standard aluminum pins. The samples on the pins were sputter-coated with gold and platinum in a vacuum system to enhance sample conductivity for SEM imaging, and then directly transferred to the SEM chamber for imaging.

Data were collected using a scanning electron microscope (FEI Quanta200FEG, Thermo Fisher, USA) equipped with a physical microtome (3View, Gatan, Pleasanton, CA, USA) inside the microscope observation chamber. An accelerating voltage of 3.5 keV, a spot size of 3, a scanning speed of 2 µsec/pixel and the high vacuum mode were used. After each iterative removal of an ultrathin slice (70 nm thick) by a diamond knife within the SEM chamber, the surface of the remaining block (specimen) was imaged. Images with 8192 x 8192 or 4096 × 4096 pixels were collected at 7-10 nm/pixel along both the x- and y-axes using the Digital Micrograph software (Gatan). Image series of regions of interest were further processed, digitally aligned and reconstructed into 3D z-stacks/tomograms using the TrakEM2 module of Fiji (https://fiji.sc).

To enable correlative TEM, once a region of interest containing inclusion bodies was identified and partly imaged by SEM, the sample was removed from the SEM chamber and cut using a physical ultramicrotome (Ultracut EM UC7; Leica Microsystems, Germany). The resulting 30-50nm-thick slices obtained were sequentially collected on EM grids (EMS Diasum) with a carbon-stabilized formvar film, and imaged at room temperature (RT) using a Philips CM10 electron microscope operated at 80 kV. Electron micrographs were recorded on a 2,048 × 2,048-pixel charge-coupled device camera (Veleta; EMSIS GmbH, Germany). Color annotation of the resulting 2D micrographs was performed manually using Adobe Photoshop CS6 (Adobe Systems Incorporated).

Lipid-aSyn Co-Staining and Fluorescence Imaging

Tissue sections (10 µm thick) of a snap-frozen tissue slice of the hippocampus (including CA2) of Patient A and the SN of Patient B were cut using a cryostat (Leica) collected on glass slides at -18 ºC, shipped on dry ice from the VUmc to C-CINA, and subsequently stored at -80 ºC. Immediately after removal from -80 ºC, slides were fixed with 4% paraformaldehyde (PFA) for 30 minutes in a humidity chamber. They were then rinsed in PBS and treated with 0.5% Triton X-100 in PBS, washed with PBS and incubated for 2 h at RT with a primary antibody to aSyn, LB509 (amino acid 115-122; abcam ab27766). After washing with PBS, slides were incubated for 1.5 h at RT with a cocktail of secondary fluorescence-conjugated antibody Alexa488 and DAPI (4',6-diaidino-2-phenylindole, dilactate; BioLegend) to visualize nuclei. Slides were washed with PBS, and then treated with Nile Red stain (Sigma 19123) for 10 min in the dark. Nile Red powder was originally diluted to 0.5 mg/ml in acetone to make a stock solution, and a fresh working solution was prepared every time by diluting an aliquot of this stock 1:200-fold in 75% glycerol. Stained slides were washed in 75% glycerol, treated with Sudan Black in the dark, rinsed in PBS and mounted in Mowiol coverslip mounting solution. They were allowed to dry in the dark overnight, and then stored at 4ºC in the dark prior to imaging.

Confocal fluorescence images (1024 x 1024 pixels) were mainly acquired at a magnification of 40x, using a point-scanning confocal microscope (CLSM Leica TCS SPE with a DMI4000 microscope) equipped with advanced correction system (ACS) objectives and the solid-state laser system: 405 nm (DAPI), 488 nm (Alexa488), and 635 nm (Nile Red). Composite images and co-localizations were calculated and created using standard tools in the Imaris software (Bitplane AG) and final figures were composed in Adobe Photoshop CS6 (Adobe Systems Incorporated). Untreated tissue samples were checked by LM before and after staining/labeling to look for auto-fluorescence, as this could interfere with label detection, and then by confocal laser scanning microscopy (CLSM) to visualize greater detail in 2D and 3D. As a further control, tissue sections were treated with the secondary fluorescence antibody alone, without the primary antibody, and examined by LM and CLSM to check for unspecific labeling.

Co-labeling for STED Microscopy

Multiple labeling experiments were performed on formalin-fixed, paraffin-embedded 20µm-thick midbrain and hippocampus sections, using markers for organelles and aSyn. For heat-induced antigen retrieval, sections were placed in sodium citrate buffer (pH 6.0) in a steamer at 90-99 °C for 30 min. Antibodies against VDAC-1/Porin (Abcam ab14734), LAMP-1 (Abcam ab24170) and S129-phosphorylated α-synuclein (pSer129 Ab 11A5, courtesy of Prothena Biosciences Inc) directly labeled with AlexaFluor 488 were used. Abberior STAR 580 and STAR 635P fluorophores (Abberior, Bioconnect) were used as secondary antibodies. Nuclei were visualized by DAPI staining (Sigma).

STED microscopy was performed on a Leica TCS SP8 STED 3X microscope (Leica Microsystems). Sections were irradiated with a pulsed white light laser at wavelengths of 499, 587, and 633 nm. A pulsed STED laser line at a wavelength of 775 nm was used to deplete the Abberior fluorophores (580, 635P), and a continuous wave (CW) STED laser with a wavelength of 592 nm was used to deplete the Alexa 488 fluorophore. Further, to obtain confocal images of the DAPI signal, sections were irradiated with a solid state laser at a wavelength of 405 nm. The DAPI signal was not depleted. All signals were detected using a gated hybrid detector in counting mode. Images were acquired using a HC PL APO CS2 100 × 1.4 NA oil objective lens, and the resolution was set to a pixel size of 20 nm x 20 nm. Finally, deconvolution was performed with Huygens Professional (Scientific Volume

Imaging; Huygens, The Netherlands). Images were adjusted for brightness/contrast in ImageJ (National Institute of Health, USA), and final figures were composed using Adobe Photoshop CS6 (Adobe Systems Incorporated).

Liquid Chromatography Mass Spectrometry and Lipidomics of Microdissected Tissues

Cryostat-cut tissue sections (7 µm) of the hippocampus (mid) of Patient A, the mesencephalon of Patient B, and the corpus callosum of a non-demented control donor (Patient C) were collected at -18 ºC. Sections were stained with haematoxylin (Sigma) for 1 min, washed under tap water for 5 min, quickly washed in sterile water, then stained with Eosin for 10 sec. They were washed in 96% EtOH for 30 seconds, 100% EtOH for 30 sec, then air-dried under a chemical fume hood prior to laser-capture microdissection (LCM). For the second LCM run, adjacent 7µm-thick sections of the Patient A hippocampus were immunostained with an antibody against aSyn FL-140 (sc-10717, Santa Cruz; dilution 1:2000) for 30 min after fixation with 96% EtOH. After rinsing with PBS, the immunostaining was visualized with Envision detection systems peroxidase/DAB (DAKO). Sections were rinsed again with Tris-HCl (pH 7.4) and running tab water, subsequently air-dried and stored at 4 ºC.

LCM was used to obtain approximately 3000 LB from the CA2 of Patient A and 2700 LB from the SN of Patient B. In both cases, LB were cut out from inverted adjacent tissue polyethylene naphthalate (PEN) membrane slides positioned on the stage of a LMD6500 (Leica Microsystems) microscope, collected in the cap of either 0.2 or 0.5 ml Eppendorf tubes, and kept on ice until further processing for mass spectrometry.

For mass spectrometry, 40 – 60 µl of chloroform:methanol 2:1 (v/v) was carefully added to the inverted caps and shaken gently to dissolve the collected LB patches. The closed tubes were inspected using a magnification glass to ensure that there was no undissolved material. When this was the case, they were analyzed by liquid chromatography mass spectrometry (LC-MS). A Dionex Ultimate 3000 RSLC nanoUPLC system with Reprospher 100 Si column (3 µm, 150 x 0.4 mm, 100 Å, Dr. Maisch GmbH, Ammerbuch-Entringen, Germany) was used to separate the isolated material by normal phase LC. The column temperature was set to 40 °C with a flow rate of 10 µL/min. Mobile phase A was isopropanol:hexane:100 mM ammonium carboxylate 58:40:2 (v/v/v) and mobile phase B was isopropanol:hexane:100 mM ammonium carboxylate 50:40:10 (v/v/v)[41]. After an initial phase at 40% B for 5 min, the gradient was ramped up from 40% to 100% B over 25 minutes and followed by a steady phase at 100% B for 5 min.

To identify the eluting peaks, the capillary nanoUPLC was connected to a Waters Synapt G2 HRMS mass spectrometer. The mass signals and their fragments were obtained by a MS scan and a survey MS/MS scan method. A standard off/axis ESI source was used as an atmosphere-vacuum interface. The spray voltage was set to 2.8 kV, the desolvation temperature was set to 200 °C, and the source temperature was set to 100 °C. The MS/MS spectra were obtained using mass-dependent collision energies. Waters Masslynx and Progeenesis QI software was used to evaluate the data.

Correlative CARS/FTIR and Immunofluorescence Imaging

Cryostat-cut tissue sections (10 µm) of the CA2 of Patient A, SN of Patient B and white matter of Patient C were collected at -18 ºC in the same manner as prepared for confocal immunofluorescence (IF) imaging, and dried under a stream of dry air at RT before coherent anti-Stokes Raman scattering (CARS) or Fourier transform infrared spectroscopy (FTIR) imaging. No stain was applied prior to imaging. Only data from Patient A is shown (Fig. 5).

CARS images were acquired using a commercial setup consisting of a picosecond-pulsed laser system that generates two synchronized beams collinearly aligned in an inverted confocal microscope (TCS SP5 II CARS; Leica Microsystems, Heidelberg, Germany). In this setup, a fraction of the fundamental light of an Nd:YVO4 (HighQ Laser, Rankweil, Austria) at 1064 nm is coupled into the microscope and used as a Stokes beam in the CARS process. The frequency-doubled output (532 nm) is used to synchronously pump an optical parametric oscillator (picoEmerald; APE, Berlin, Germany), tunable in the 780–960 nm range. The laser beams are focused into the tissue by an HCX IRAPO L water immersion objective (25x/0.95 W CORR; Leica Microsystems). The forward-detected CARS signal is measured via a non-descanned detector. The mean laser power was measured at the tissue position and found to be 28 and 21 mW at 816 and 1064 nm, respectively. A typical pixel dwell time of 32 µs per scan was selected (31 s per image, 1024 x 1024 pixels covering up to 300 x 300 µm sample area, pixel resolution 300 nm[42]. CARS images of tissues were measured at 816 and 806 nm, which correspond to 2850 cm^{-1} (lipids, CH_2) and 2930 cm^{-1} (proteins, CH_3). The lipid and protein distribution profiles in LB were calculated using the Image Processing and Statistic toolboxes of Matlab (The Mathworks, Inc., Mass., USA).

For the FTIR measurements, infrared hyperspectral data acquisition was performed in transflection mode using an Agilent Cary 620 microscope with an Agilent Cary 670 spectrometer (Agilent, California, USA). Spectral data were collected by an MCT focal plane array detector with 128 x 128 elements, providing a field of view (FOV) of approximately 422 µm x 422 µm with a 25x magnification (NA 0.82). The spectral data were collected from 3700 - 950 $cm^{-1}$with a spectral resolution of 4 cm^{-1}. Fourier transformation was performed with a Mertz phase correction, Blackman-Harris 4-term apodization, and a zero filling of 2. A high numeric aperture of 0.82 was used[43]. Tissue sections were prepared on LowE slides for the transflection (reflection-absorption) measurements. The second derivative that minimizes the effects of the standing wave artifact was tested in addition. This resulted in the same spectral band positions. Therefore, the vector-normalized spectra were used.

The resulting raw spectral maps were pre-processed using the previously described workflow[44]. Strong artifacts possibly arising from cracks or folds in the tissue were eliminated by quality control based on the signal-to-noise ratio and the integral of the amide I band. The remaining spectra were subjected to a Mie and resonance-Mie correction based on Extended Multiplicative Signal Correction, EMSC[45] in the wavenumber range from 3100 to 950 cm^{-1}. The correction was performed with 30 iteration steps. Higher numbers of iteration steps (up to 100) were tested but the resulting spectra did not show further variances.

For immunofluorescence staining, after CARS or FTIR imaging tissue sections were kept on the slides and fixed with 4% formaldehyde for 30 min. Slides were rinsed and shipped in PBS, then treated with 0.5% Triton X-100 in PBS for 10 min. Slides were rinsed with PBS before incubation for 2 h at RT with an antibody targeting phosphorylated aSyn, phospho-S129 (pS129; abcam ab59264). After washing with PBS, sections were incubated for 1.5 h at RT with a secondary fluorescent antibody (Alexa488), rinsed again with PBS and applied with the next primary antibody to aSyn, LB509 for another 2 h at RT. After rinsing with PBS, sections were incubated for 1.5 h at RT with a secondary fluorescent antibody (Alexa647), rinsed in PBS, and applied with Sudan Black for 30 min. After rinsing again in PBS, they were finally mounted in Mowiol and allowed to dry in the dark overnight, subsequently being stored at 4 ºC.

Brightfield and immunofluorescence images corresponding to each CA2 region imaged by CARS or FTIR were collected at 10x magnification using a confocal microscope (Leica TCS SP5 CARS with a DMI3000). Images from brightfield/immunofluorescence and CARS

or FTIR were overlaid and aligned to each other based on the morphology of tissue edges and lipofuscin deposits that appeared as black granules in the cell soma. Images were collected using an Ar-laser with 488 nm (Alexa488) excitation. An overlay of CARS or FTIR images with their counterparts showing aSyn immunofluorescence was performed using Adobe Photoshop CS6 (Adobe Systems Incorporated).

Acknowledgements

We are grateful to the individuals who participated in the brain donation program and their families, making this study possible. We thank Ariane Fecteau-LeFebvre for EM maintenance, Allert Jonker and Jeroen J.M. Hoozemans for help with preparing cryostat-cut tissue sections, Daniel Mona for help with the antibodies, Paul Baumgartner and Karen Bergmann for administrative help, and Shirley Müller for carefully proof-reading and editing the manuscript. S.H.S. was supported by the Roche Postdoctoral Fellowship (RPF) program; this work was in part supported by the Swiss National Science Foundation (SNF Grant CRSII3_154461) and the Synapsis Foundation Switzerland.

Author Contributions

S.H.S. performed CLEM/TEM and tomography, SBFSEM imaging and 2D/3D color segmentations, analyzed data, and wrote the manuscript; C.G. and A.G.M. trained and supported S.H.S. with SBFSEM tissue preparation and imaging; Jü.H. screened LM slides and analyzed LM data of CLEM for localizing LB/LN; Jü.H., G.S. and S.I. designed and optimized the staining for CLEM and localization of LB/LN in LM data with S.H.S.; W. vdB., T.M. and E.H. performed STED imaging; J.W. and K.N.G. assisted with TEM tomography; R.S. and S.H.S. optimized and performed lipid and aSyn co-staining and confocal imaging; D.C. performed sub-tomogram analysis; P.P.N. helped acquire SBFSEM control data (not shown); A.I. processed tissue samples collected at the autopsy room, prepared cryostat tissue and sectioned paraffin embedded tissue; Y.dG. prepared cryostat tissue for CARS and FTIR imaging; A.J.M.R., and W.vdB. performed rapid autopsies of PD patients and controls, collected brain tissue and preformed neuropathological assessment; W.vdB. guided neuroanatomical imaging, and performed laser-capture micro dissection with S.H.S.; A.D.P. performed Raman imaging tests; J.E., A.S. and Joerg H. performed LC-MS analysis; D.N., S.F.EM. and K.G. performed and analyzed CARS imaging; F.G. performed FTIR imaging; M.Q., W.F.J.vIJ. and V.B. provided whole exome sequencing and genetic analysis of PD patients; B.B. provided technical input to EM analysis of brain tissue in neurodegeneration; S.F. provided expertise in neuropathology, differentiation of LB *vs.* CA, and provided optical microscopy data of CA and LB in same tissues; M.B., H.S., W.vdB., and M.E.L. designed research, analyzed and interpreted the data, and contributed to writing the manuscript.

Competing financial interests

The authors declare no competing financial interests. A.d.P., J.E., A.S., J.H., B.B., M.B., and M.E.L. are full-time employees of Roche/F. Hoffmann–La Roche Ltd, and they may additionally hold Roche stock/stock options.

Corresponding authors

Correspondence to: Matthias Lauer (matthias.lauer@roche.com), Wilma van de Berg (wdj.vandeberg@vumc.nl), Henning Stahlberg (henning.stahlberg@unibas.ch), and Markus Britschgi (markus.britschgi@roche.com)

Tables

Patient ID	Diagnosis	Age at onset	Age at death	Sex	Brain weight (g)	PMD (hrs)	Braak NFT stage	CERAD (Abeta) score	Braak aSyn stage	Thal phase	CAA
Patient A	PDD	59	77	M	1240	5:15	2	0	6	3	Type 2
Patient B	PDD	75	90	F	1335	4:45	3	B	6	3	Type 2
Patient C	NDC	n.a.	72	F	1205	5:15	1	A	0	1	Type 1

Table 1. Clinical and pathological characteristics of brain donors. PDD=Parkinson's disease with dementia; n.a. = not applicable; NDC = non-demented control; NFT = neurofibrillary tangles; CERAD = Consortium to Establish a Registry for Alzheimer Disease, CAA = cerebral amyloid angiopathy; aSyn = α-synuclein; PMD = postmortem delay.

Figures

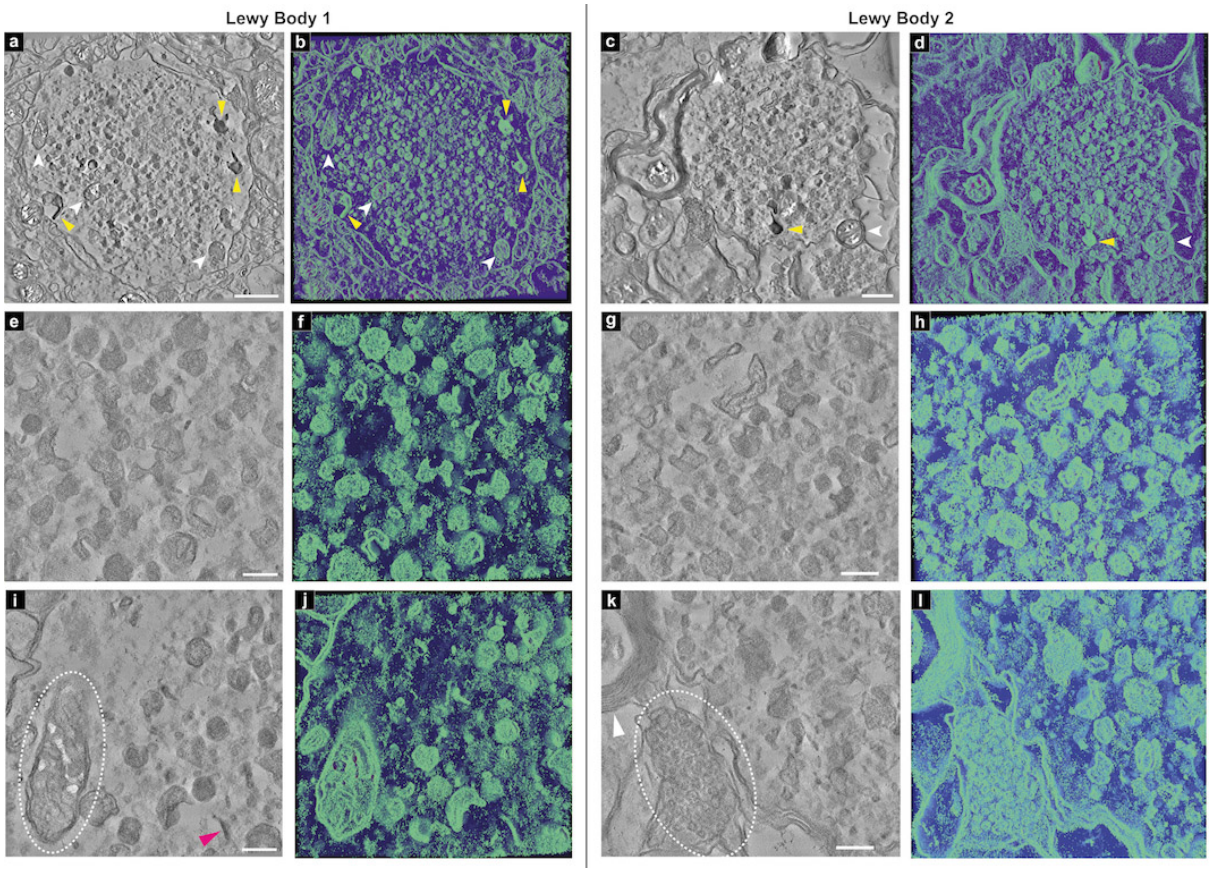

Figure 1. Electron tomography reveals abundant membranous structures, abnormal organelles and vesicles in nigral Lewy bodies. Projections of the indicated number of central slices of the reconstructed 3D tomograms are shown. Corresponding to Patient A, hippocampal CA2. (a) "LB1" and the surrounding cellular milieu (central 20 slices); white arrowheads indicate mitochondria, yellow arrowheads indicate densely compact membranous structures. (b) 3D color segmentation of the reconstructed tomogram with the same features marked. (c) "LB2" and the surrounding cellular milieu (central 60 slices); the arrowheads indicate a mitochondrion (white) and densely compact membranous structures (yellow). (d) 3D color segmentation of the reconstructed tomogram with the same regions marked. (e) Inner region of the LB shown in 'a' (LB1; central 60 slices). Distorted vesicular structures are present. (f) 3D color segmentation of the same reconstructed tomogram. (g) Inner region of the LB shown in 'c' (LB2; central 60 slices). (h) 3D color segmentation of the same reconstructed tomogram. (i) Edge of the LB shown in 'a' (LB1; central 60 slices). The upper mitochondrion indicated in 'a' is visible (white oval). The pink arrowhead indicates a disc-like membranous structure. (j) 3D color segmentation of the same reconstructed tomogram. (k) Inner region of the LB shown in 'c' (LB2; central 60 slices). Cluster of vesicular structures in adjacent yet separate compartment to the LB is visible (white oval). (l) 3D color segmentation of the same reconstructed tomogram. The tissue sample was from Patient B (Table 1). Scale bars: a = 1 µm; c = 500 nm; e, j, i, k = 200 nm.

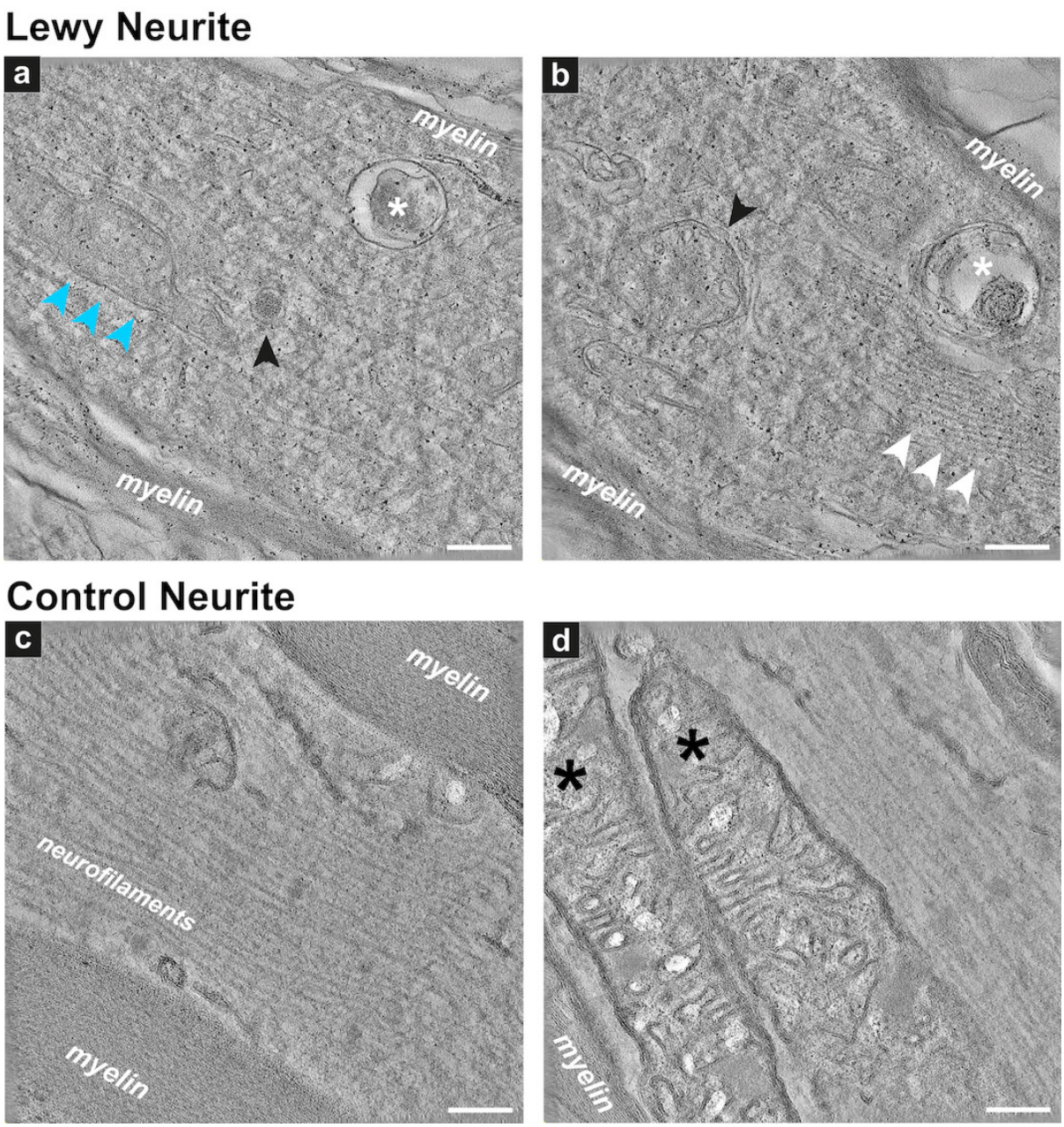

Figure 2. Electron tomography of nigral Lewy neurite revealing disrupted cytoskeletal elements, dysmorphic mitochondria and autophagosome-like structures. LN from Patient B *substantia nigra*. (a) Inner region of the LN shown in Fig. S4g (upper dotted red box). Projection through the central 40 slices of the reconstructed 3D tomogram. Elongated double-membrane enclosed structures with faint inner membrane convolutions are visible, identified as abnormally elongated and otherwise dysmorphic mitochondria (blue arrowheads). A dense-core vesicle (black arrowhead) and an autophagosome-like structure (white asterisk) are also present. (b) Different inner region of the LN shown in Fig. S4g (lower dotted red box). Projection through the central 40 slices of the reconstructed 3D tomogram. A small mitochondrion (black arrowhead) and an autophagosome-like structure (white asterisk) are present; neurofilaments (white arrowheads) are visible in one corner of the neurite. Control neurites: (c) Inner region of a "normal" neurite in the brain of a non-demented, age-matched donor (Patient C, Table 1). Projection through the central 60 slices of the reconstructed 3D tomogram. Ordered neurofilaments are visible, flanked by a well-structured myelin sheath representing the enclosing axon. (d) Inner region of a separate

neurite in the brain of a non-demented, age-matched donor (Patient C; Table 1). Projection through the central 60 slices of the reconstructed 3D tomogram. Ordered neurofilaments are visible, alongside well-structured mitochondria (black asterisk) with normal cristae. Scale bars: 200 nm.

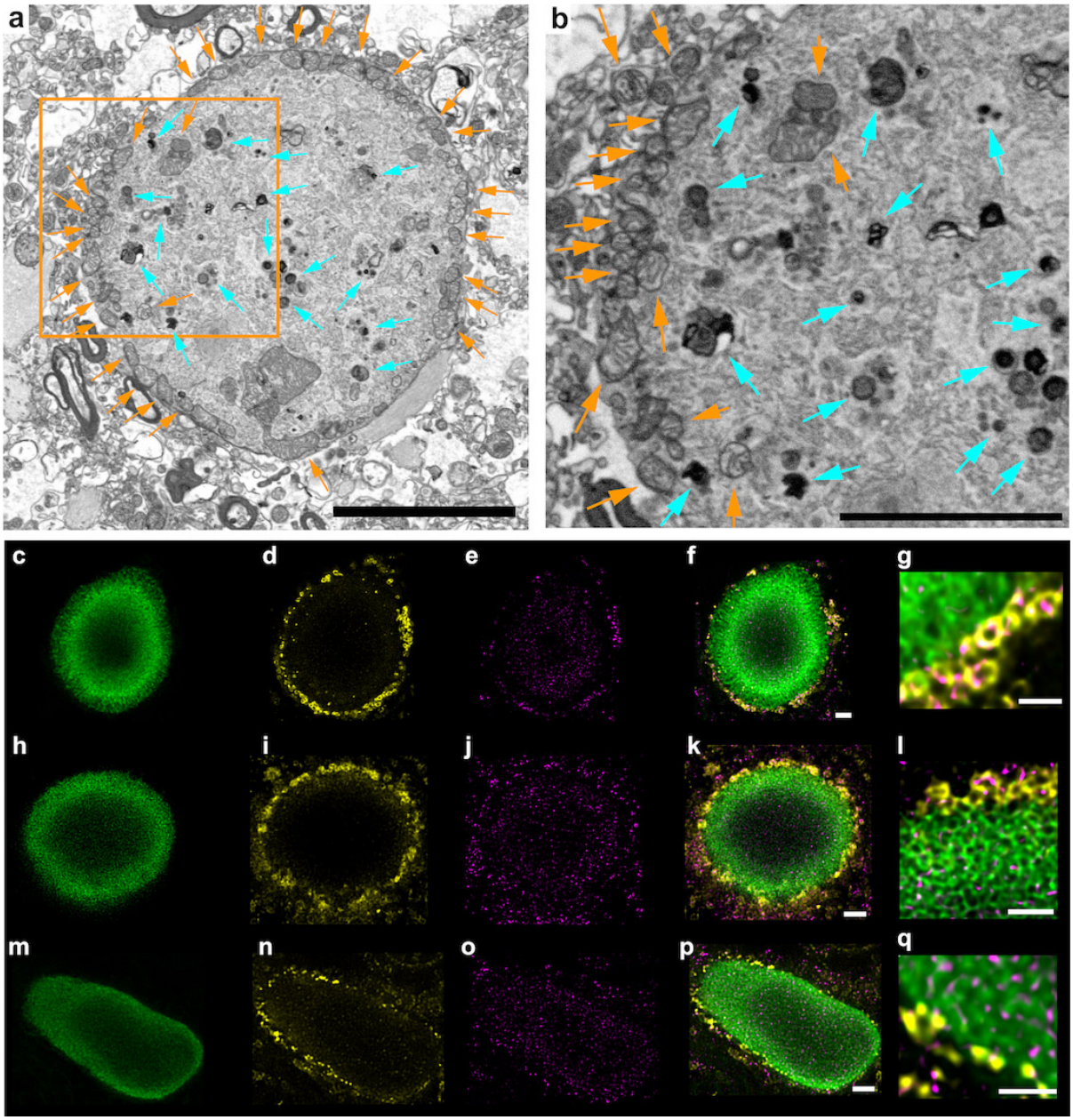

Figure 3. Sub-cellular features visualized by SBFSEM and multi-labeling STED microscopy of nigral LB and LN reveal the organelle distribution. (a) SBFSEM imaging of heavy-metal stained LB tissue showing a surrounding ring of mitochondria (orange arrows) and structures reminiscent of lysosomes/autophagosomes (aqua arrows) further within the LB. (b) Enlarged view of the boxed region in 'a', similarly annotated. (c-q) STED microscopy (c-i) of other LB and (m-q) of a LN in the same SN region of the same patient, showing the distribution of (c, h, m) marker for phosphorylated aSyn (pS129), (d, i, n) marker for mitochondria (the porin VDAC1), (e, j, o) marker for lysosomes (LAMP1), (f, k, p) overlay of all markers, (g, l, q) enlarged view of the edge of the LB in 'f' and 'k' and the LN in 'p'. Scale bars: f, k, p = 2 µm; g, l, q = 1 µm.

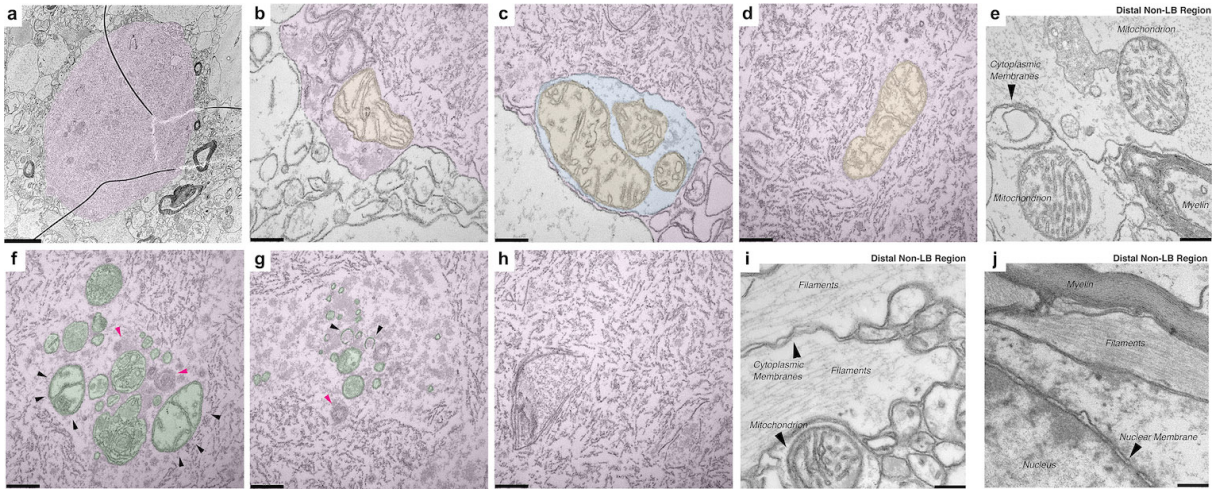

Figure 4. Inner architecture of nigral LB shows membrane fragments and organelles. TEM images of sections (50 nm thick) of an aggregate localized by SBFSEM in the SN of Patient B. Images are artificially colored: LB=pink, membrane compartments=blue, mitochondria-orange, other organelles=green. (a) Overview of the LB within the tissue. (b) Edge of the LB with a mitochondrion present. (c) Another edge of the LB with mitochondria enclosed in a membrane-delimited compartment. (d) Mitochondrion surrounded by membrane fragments within a LB. (e) Two apparently normal mitochondria with clear cristae in an area within the same tissue section but distal to the region with the LB. Cytoplasmic membranes and a myelin sheath are also present. (f) Putative mitochondria (black arrowheads) and putative lysosomes (pink arrowheads) within the LB. (g) Membrane-bound structures, some potentially omegasomes (black arrowheads) and one a putative lysosome (pink arrowhead), surrounded by fuzzy structures that may represent proteinacious deposits within the LB. (h) General cluster of membrane fragments appearing within the LB. (i) Typical cytoskeletal filaments along with mitochondrion showing clear cristae, in an area within the same tissue section but distal to the region with the LB. (j) Condensed filaments and myelin along with nuclear membrane, in an area within the same tissue section but distal to the region with the LB. Note the appearance of membranes vs. filamentous structures; the staining approach employed made it easy to distinguish between them. Scale bars: 200 nm.

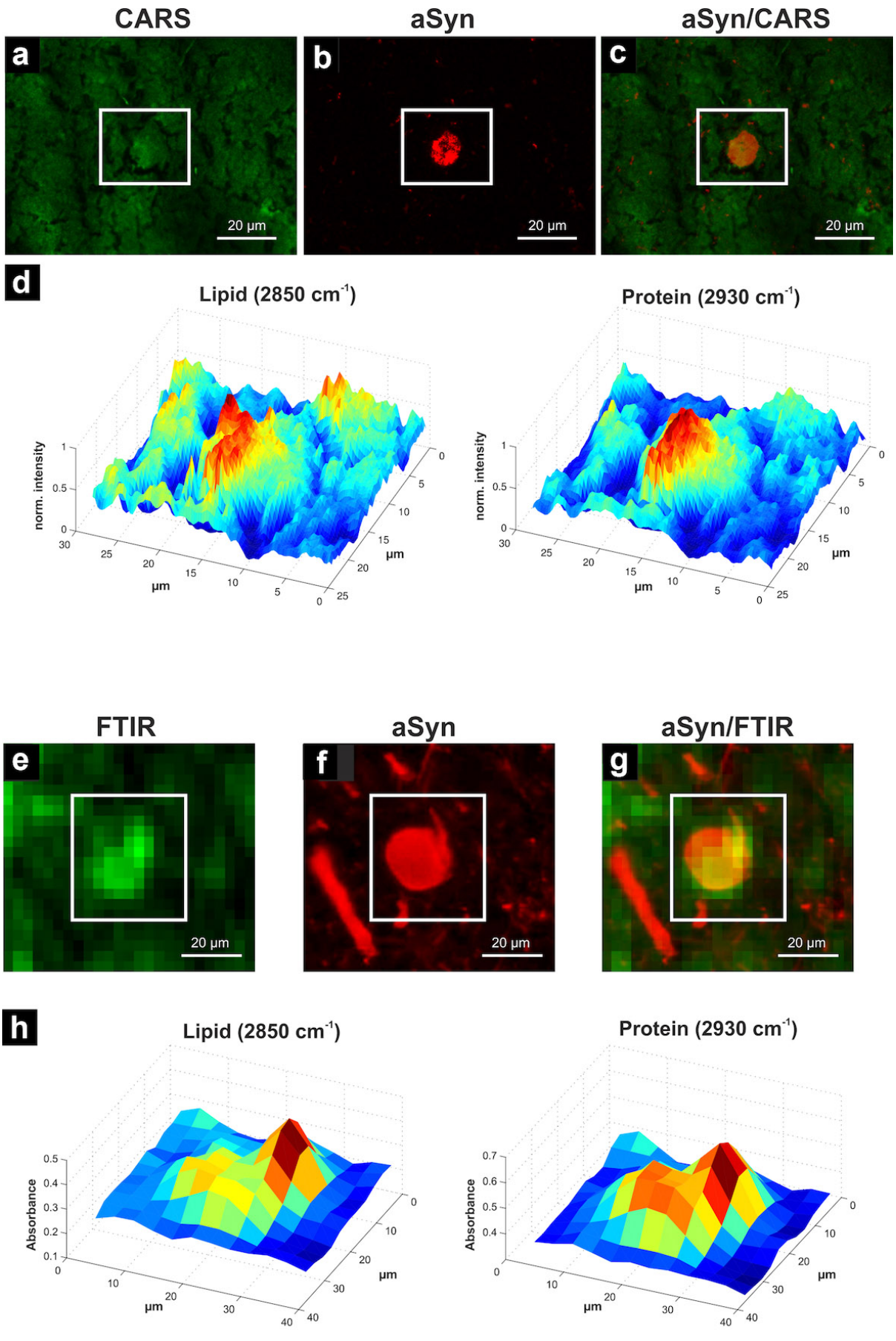

Figure 5. Lipid and protein distributions in Lewy bodies detected by label-free CARS or FTIR imaging combined with correlative immunofluorescence CLSM for aSyn. In Patient A, CA2. (a) CARS image of lipids in a LB in PD brain tissue, recorded at 2850 cm^{-1}. (b) Projected confocal immunofluorescence stack showing the same area, after immunostaining for aSyn (LB509). (c) Overlay of the CARS and aSyn immunofluorescence data shown in 'a' and 'b'. (d) CARS intensity distribution profiles for lipids and proteins within the area, showing high peaks in the region of the LB. (e) FTIR image of lipids in a LB in PD brain tissue. (f) Projected confocal immunofluorescence stack showing the same area, immunostained for aSyn (LB509). (g) Overlay of the FTIR and aSyn immunofluorescence data shown in e and f. (h) FTIR intensity distribution profiles of lipids and proteins within the LB. Scale bars: 20 μm.

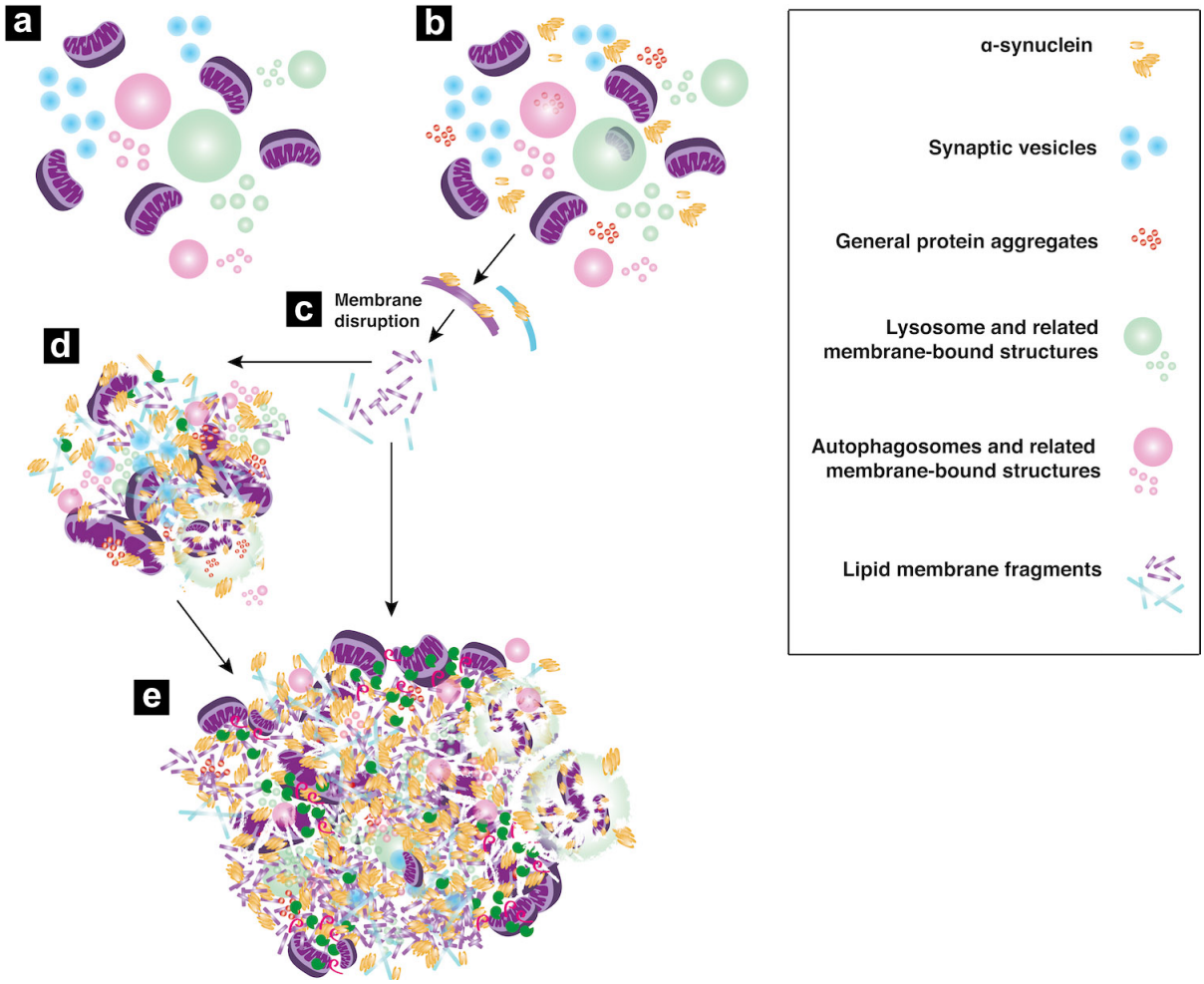

Figure 6. Hypothetical mechanism for the formation of Lewy pathology in PD. (a) Organelles including mitochondria as they exist physiologically in the cell, and (b) in the presence of pathologically aggregated or modified aSyn (e.g., phosphorylated at Ser129, oxidated, truncated, etc.) together with other protein aggregates. Over time, this may lead to (c) disruption of organellar membranes and (d) further aggregation of organelles and disruption and fragmentation of their lipid membranes. (e) Larger clumps of lipid membrane fragments, aggregated proteins, vesicles and autophagosomal and lysosomal structures, which compact over time in the restricted cellular environment giving rise to the ultrastructure of Lewy pathology observed by the CLEM methods used in this study.

Supplementary Information

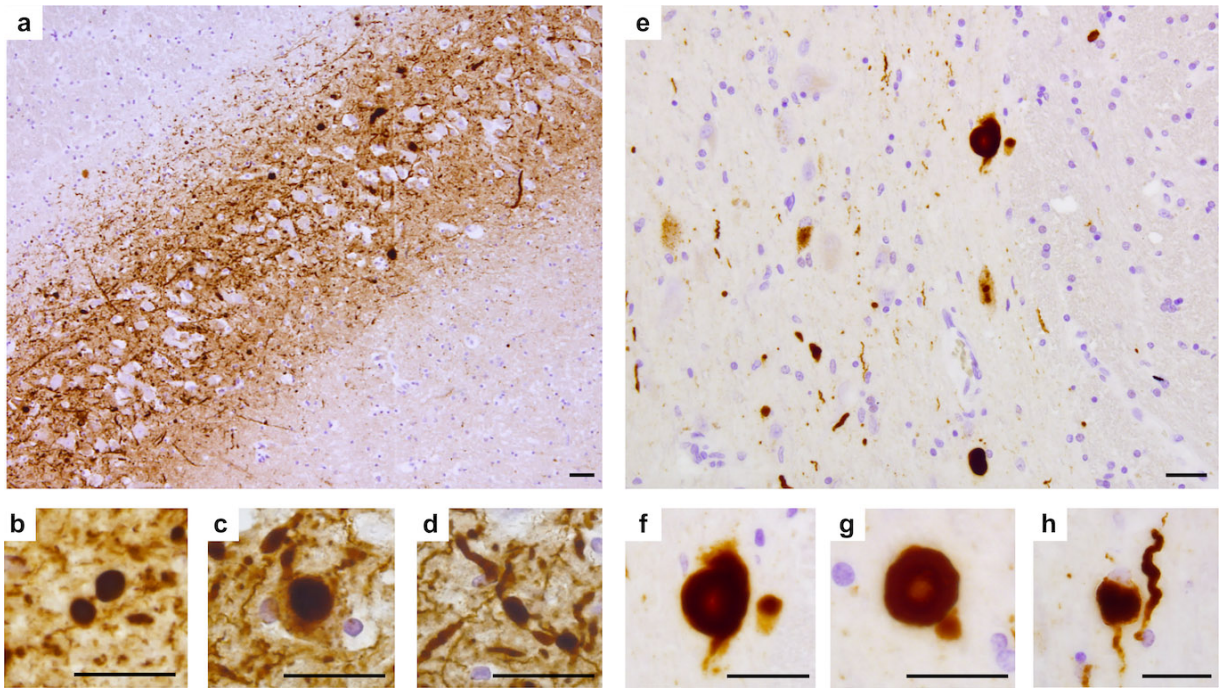

Figure S1. Immunohistochemical analysis of aSyn pathology. (**a-d**) aSyn (KM-51) immunostaining in the CA2 region of the hippocampus of Patient A. (**e-h**) aSyn (KM-51) immunostaining of the *substantia nigra* of Patient B. Images shown are from tissues that were taken from the same region of the same patients used for the other methods employed in this study, including CLEM and SBFSEM. Scale bars = 50 µm.

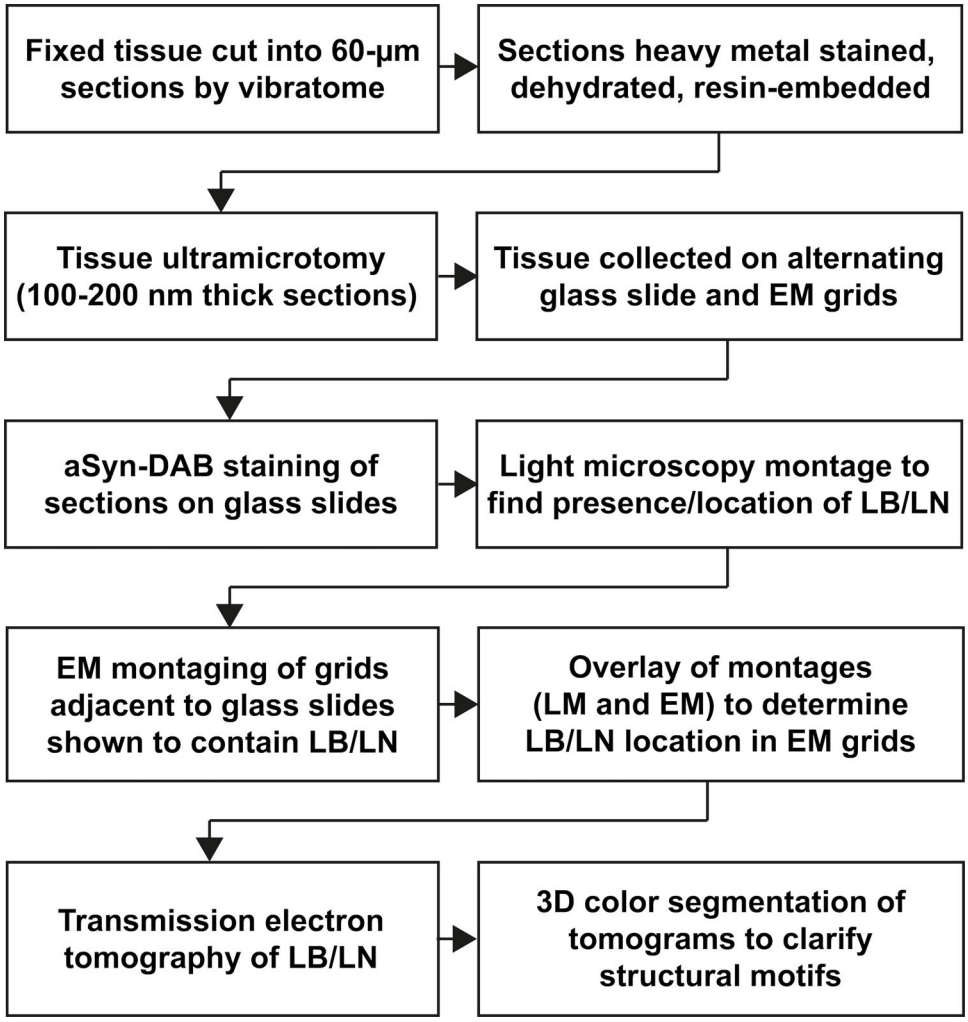

Figure S2. CLEM workflow. Correlative light and electron microscopy (CLEM) is often used to localize specific molecules of interest within the complex and diverse biological landscape of cells and tissues, typically via genetically encoded fluorescent or enzymatic markers[46]. Light microscopy is first used to visualize wide-field images with limited resolution, essentially providing a map to the labeled structures of interest. Such a map is then used to guide to the structure of interest for higher-resolution visualization by electron microscopy at a smaller imaging window. The general sequence of steps taken to achieve this for PD brain tissue sections is shown. No former ultrastructural studies have clearly demonstrated a correlative imaging approach that uses histological immunostaining for aSyn (the most widely accepted defining marker of LB) in ultra-thin sections and LM, together with EM of the same LB in subsequent ultra-thin sections. EM = electron microscopy; LM = light microscopy; aSyn-DAB = alpha-synuclein immunostaining with enzyme-linked secondary antibody and 3,3′-diaminobenzidine as chromogen; LB = Lewy body; LN = Lewy neurite.

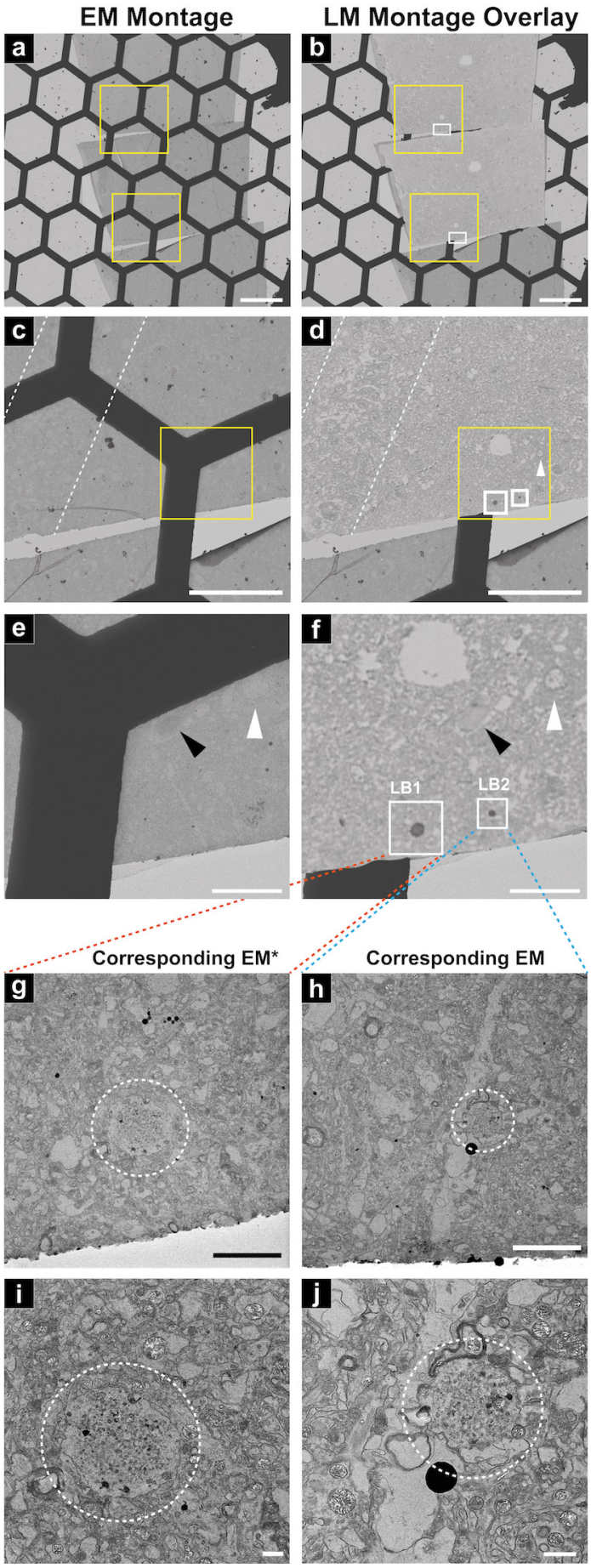

Figure S3. Correlative light and electron microscopy (CLEM) of Lewy bodies. From Patient A, hippocampal CA2. (**a**) EM montage of ultra-thin (100-200 nm) tissue sections collected on an EM grid. **(b)** Light microscopy montage of immunostained adjacent ultra-thin (100-200 nm) tissue sections, overlaid onto the EM montage. (**c**) Zoomed-in area of the lower yellow box depicted in 'a'; dotted lines indicate distinct anatomical layer of cell bodies visible by EM. (**d**) Zoomed-in area of the lower yellow box depicted in 'b'; dotted lines indicate distinct anatomical layer of cell bodies also visible by LM. (**e**) Zoomed-in area of the yellow box depicted in 'c'; white arrowhead indicates a cell nucleus with blood vessel visible (black arrowhead) by EM. (**f**) Zoomed-in area of the yellow box depicted in 'd'; white arrowhead indicates the same cell nucleus with blood vessel visible to the left (darker oval structure) by LM, matching what is shown by EM. Two LB indicated in white boxes. (**g**) Higher magnification EM image depicting a LB (LB1), white dotted circle. Since the EM grid bar obscured this LB, the actual tomogram was collected on an adjacent serial section present on the same grid. (**h**) Higher magnification EM image depicting a LB (LB2), white dotted circle. **(i)** Progressively higher magnification EM image of LB1, and **(j)** LB2. Scale bars: a, b = 200 µm; c, d = 100 µm; e, f = 20 µm; g, h = 5 µm; i, j = 1 µm.

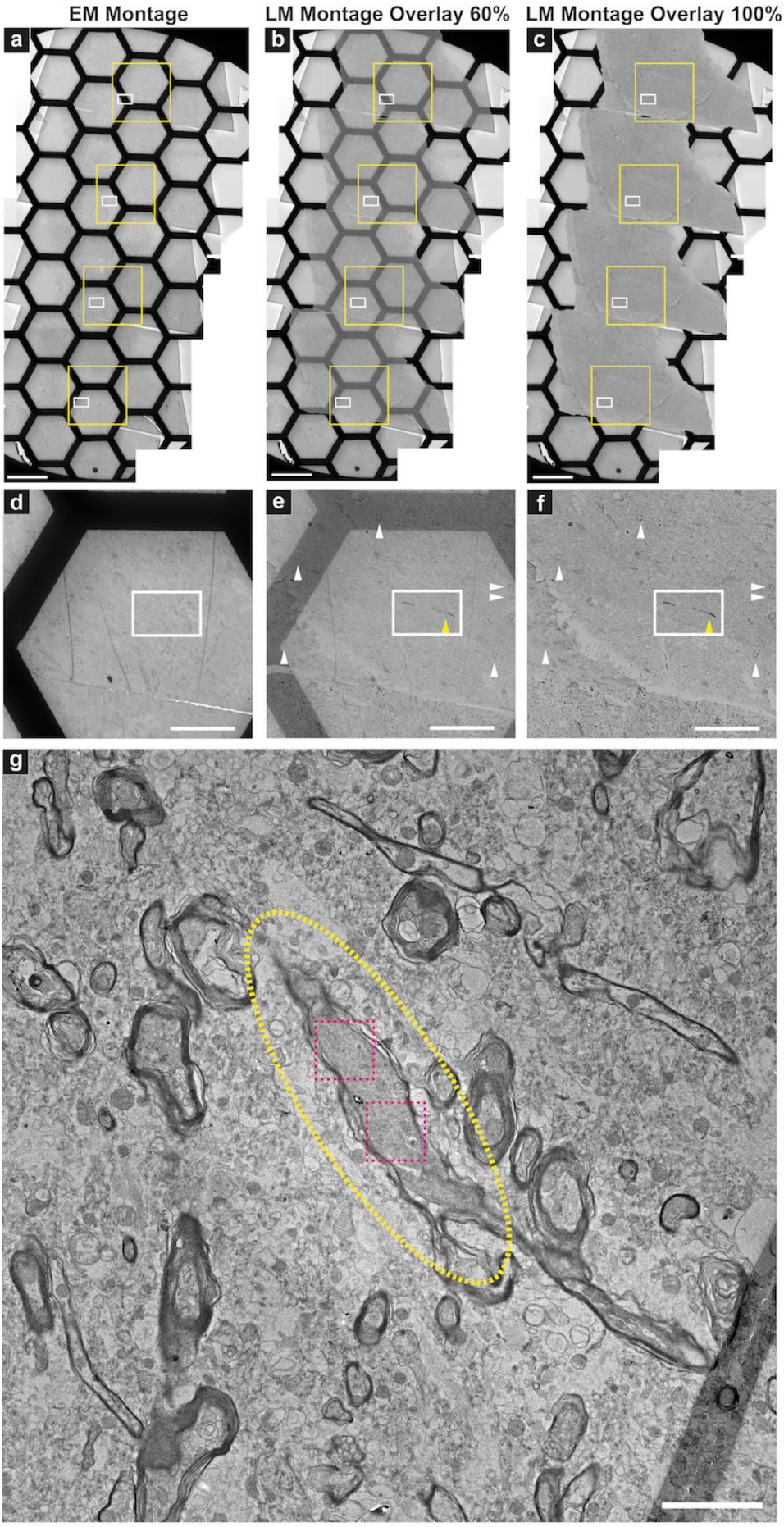

Figure S4. CLEM of Lewy neurites revealing a disrupted cytoskeletal network. From Patient B, *substantia nigra*. (**a**) EM montage of ultra-thin (100-200 nm) tissue sections collected on an EM grid. **(b)** LM montage of immunostained adjacent ultra-thin (100-200 nm) tissue sections, overlaid onto the EM montage at 60% transparency and **(c)** at 0% transparency. **(d)** Zoomed-in area of the yellow box marked with an asterisk in 'a'; the white box indicates the location of a LN, determined by overlaying the EM montage with the LM montage (**e**) at 60% and (**f**) at 0% transparency, and aligning them based on the position of the cell nuclei (white arrowheads), which can be seen by both microscopies. Part of the LN (yellow arrowheads) was selected for subsequent electron tomography. This particular boxed region was chosen for tomography since there were no obscuring grid bars present. (**g**) Higher magnification EM image indicating the LN (yellow dotted oval) shown by the yellow arrowheads in 'e' and 'f', and the specific positions where electron tomograms were collected (pink dotted boxes). Scale bars: a, b, c = 200 µm; d, e, f = 50 µm; g = 3 µm.

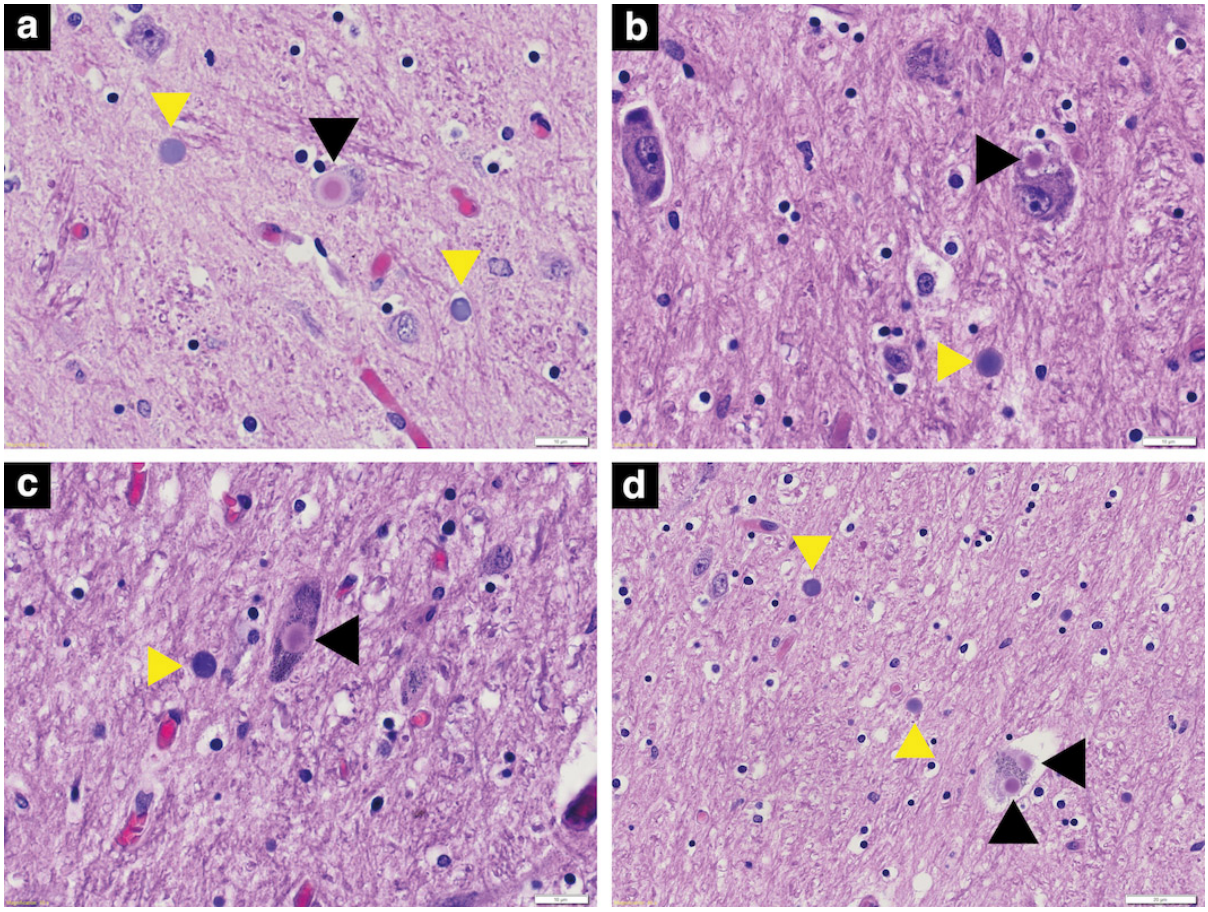

Figure S5. Conventional histopathological aspect of FFPE sample of the *Substantia nigra* obtained from a PD patient shows Lewy bodies and *Corpora amylacea* side by side. (**a-d**): H&E stained tissue sections; yellow arrowheads indicate *CA*; black arrowheads indicate LB. Note the similar size of the two structures and that they can occur in close proximity to one another, even though *CA* are extracellular. Lewy himself noted the potential conundrum of distinguishing between the two[47], and it remains a challenge today. As documented by later results sections, detailed CLEM microscopy (Fig. S2) was critical to distinguish the two with certainty. No former ultrastructural studies report the use of a comparable correlative imaging approach. Thus, it cannot be excluded that some of the structures previously analyzed by EM and published as a characterization of LB were in fact *CA*. Furthermore, the relatively high abundance of *CA* in the majority of aged brain samples compared to the low spatial density of LB, even in advanced PD, makes it statistically unlikely to cut through a LB when sectioning tissue samples of the size typically embedded for EM. Scale bars: a-c = 10 µm; d = 20 µm.

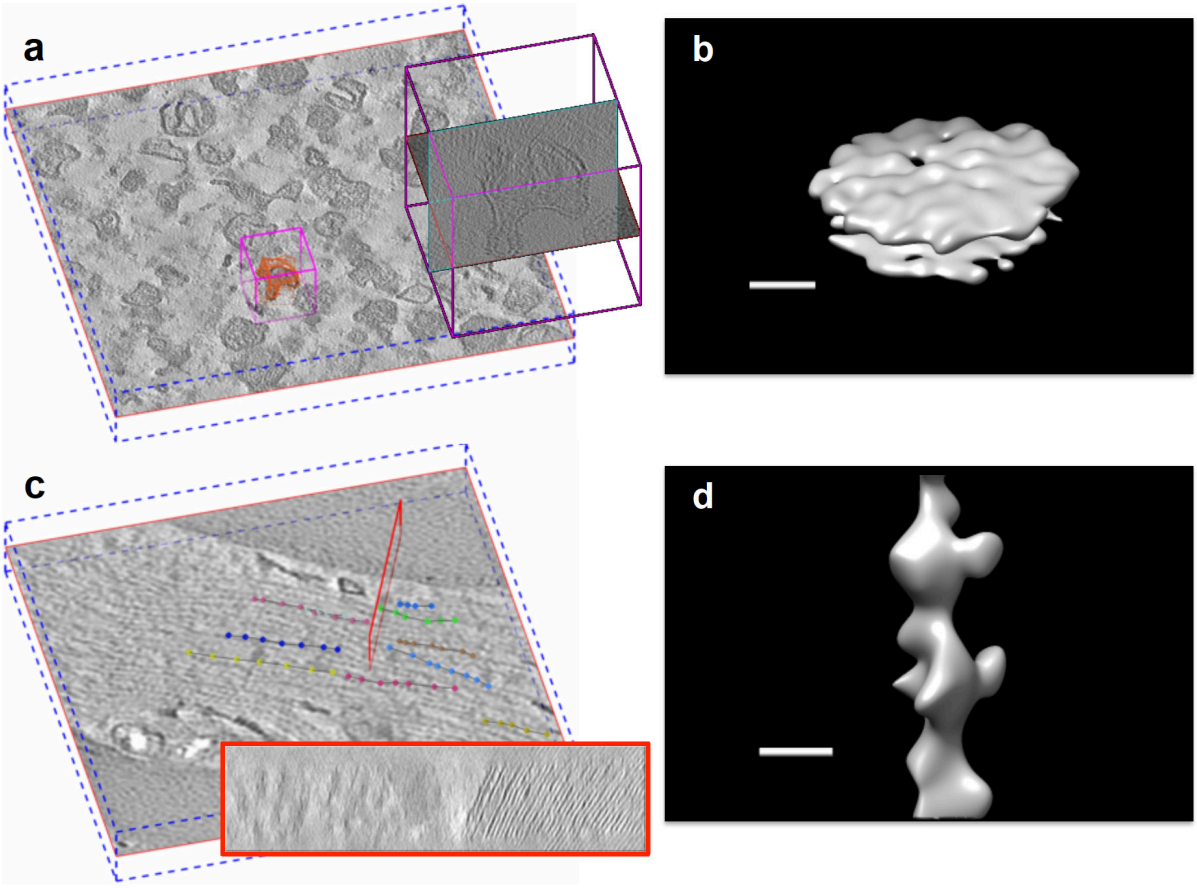

Figure S6. Membrane structure within a nigral Lewy body revealed by electron tomography and sub-volume averaging compared to a filament structure from a 'control' neurite. (**a**) Z-orthoslice in a tomogram from a LB and the region selected for sub-tomogram averaging (pink box). Sub-volumes were sampled on high intensity points around the indicated locations (red). (**b**) Sub-volume averaging for the sampled densities in the LB revealed a membrane structure with the two leaflets separated by the typical spacing of a lipidic bilayer. (**c**) Z-orthoslice in a tomogram from a neurite of a non-demented, age-matched 'control' patient. The red box indicates a cross-section showing myelin sheaths (right side of box) and filaments (left side of box) within the neurite. (**d**) Averaging sub-volumes sampled along the dotted lines in 'c' revealed a filamentous structural signature. Scale bars = 10 nm.

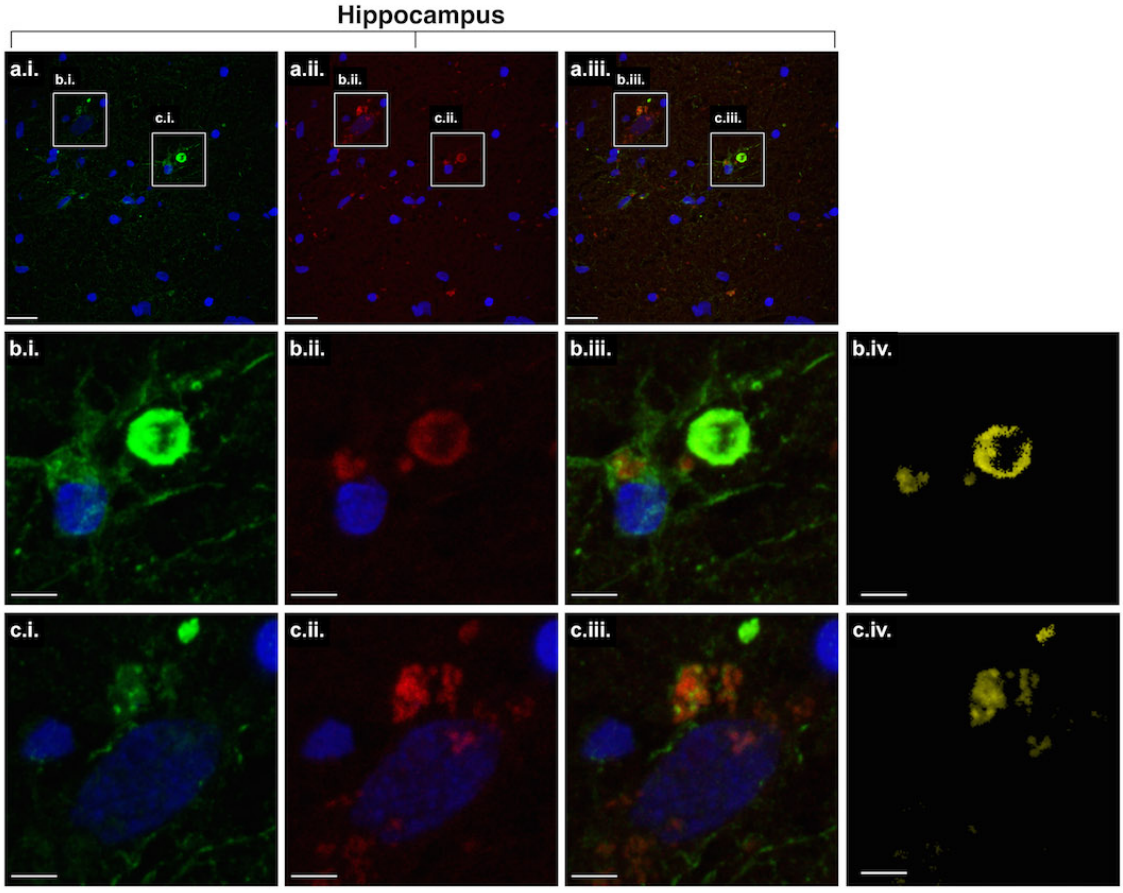

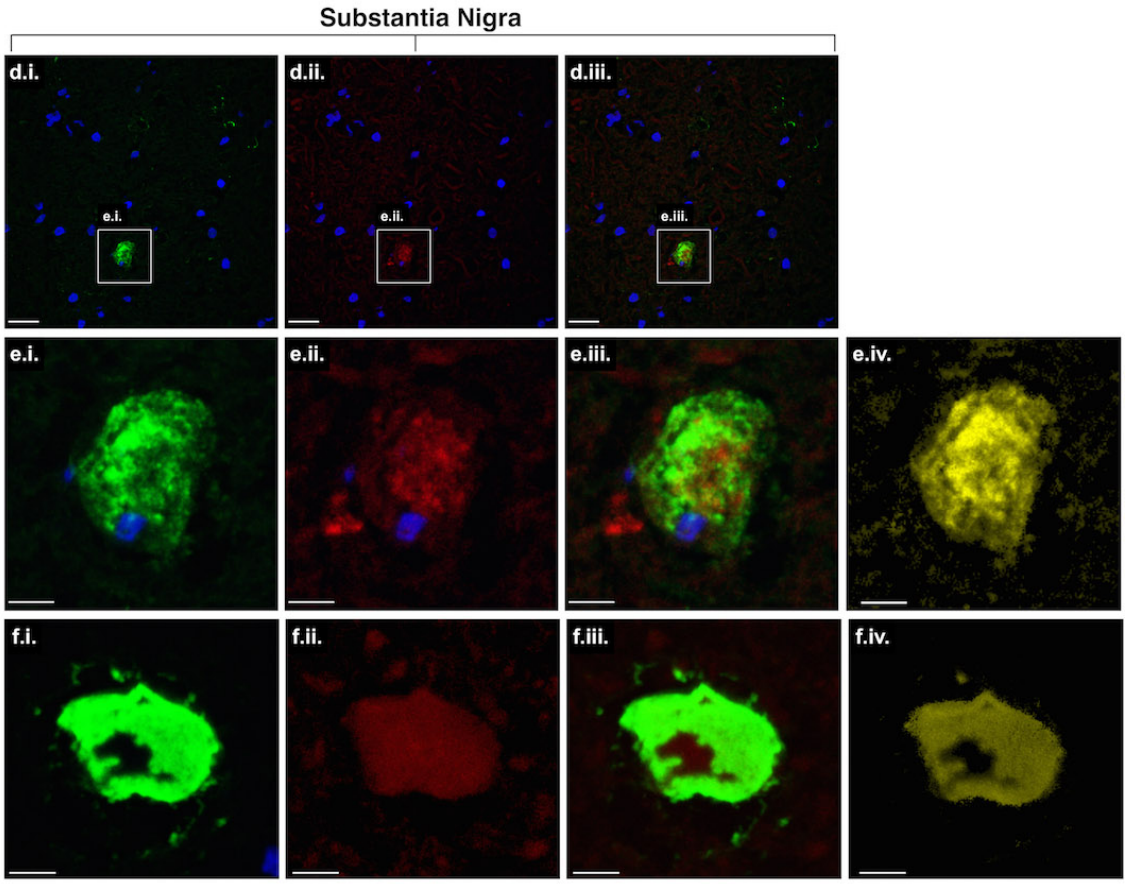

Figure S7. Co-localization of lipids with aSyn in Lewy bodies by confocal fluorescence light microscopy. Confocal projected image stacks of snap-frozen 10µm-thick tissue showing LB in the (**a-c**) hippocampal CA2 region of Patient A, and (**d-f**) SN of Patient B. Structures immunopositive for aSyn are visualized in green (LB509 antibody), lipid-rich structures are visualized in red by Nile Red staining, and nuclei are visualized in blue by DAPI. Column i = aSyn (green), nuclei (blue); Column ii = lipids (red), nuclei (blue); Column iii = overlay of aSyn (green), lipids (red), and nuclei (blue); Column iv = co-localization of aSyn and lipids (yellow). Scale bars: a, d = 20 µm; b, c, e, f = 5 µm.

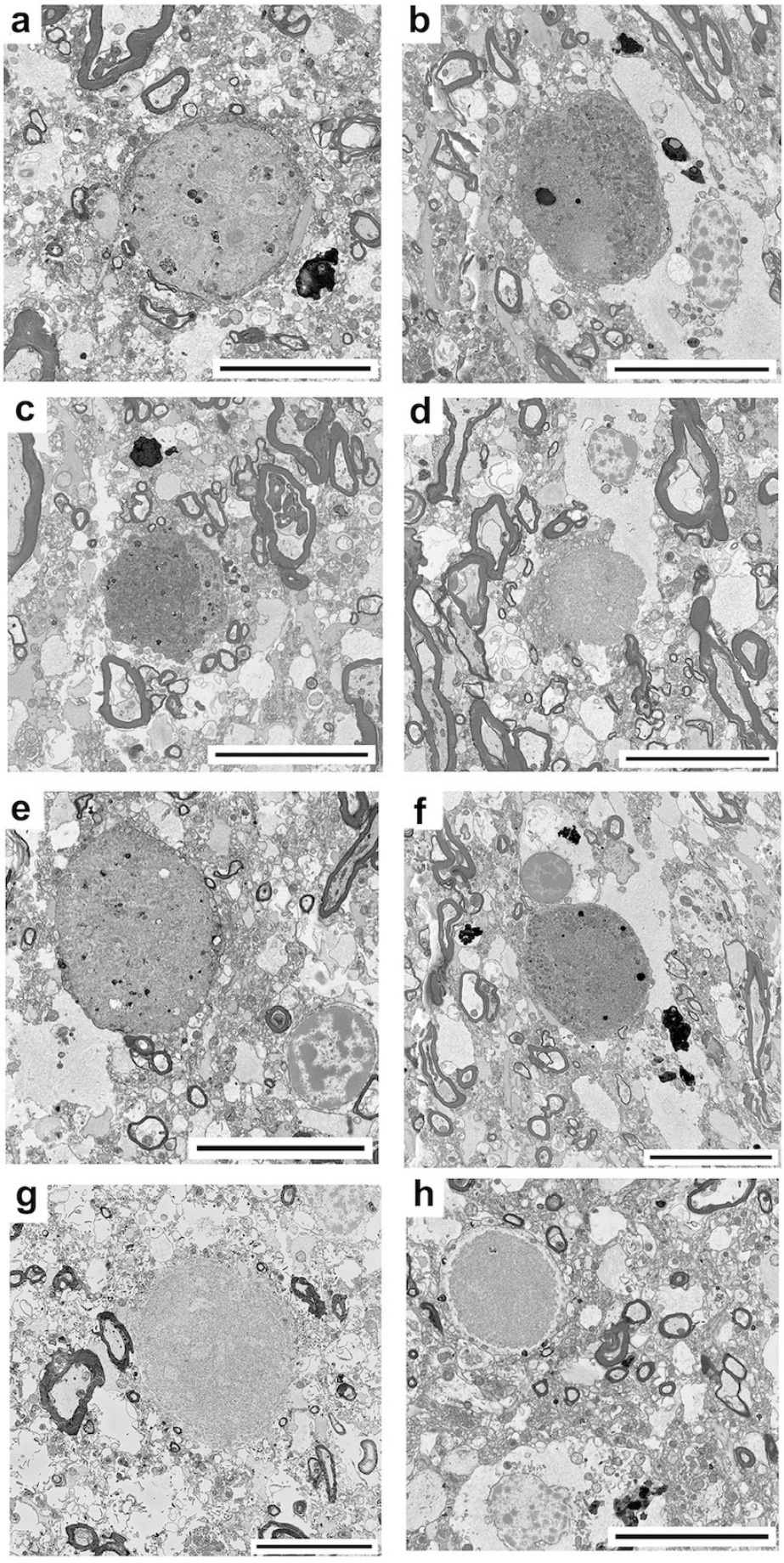

Figure S8. Distribution and morphology of heavy metal-stained cellular aggregates in SN as visualized by SBFSEM. (**a-h**) Various aggregates of similar size, shape and tissue localization relative to LB as visualized by complementary techniques, located in the SN of Patient B. Each image represents one slice from a 3D reconstructed stack. Scale bars: 10 µm.

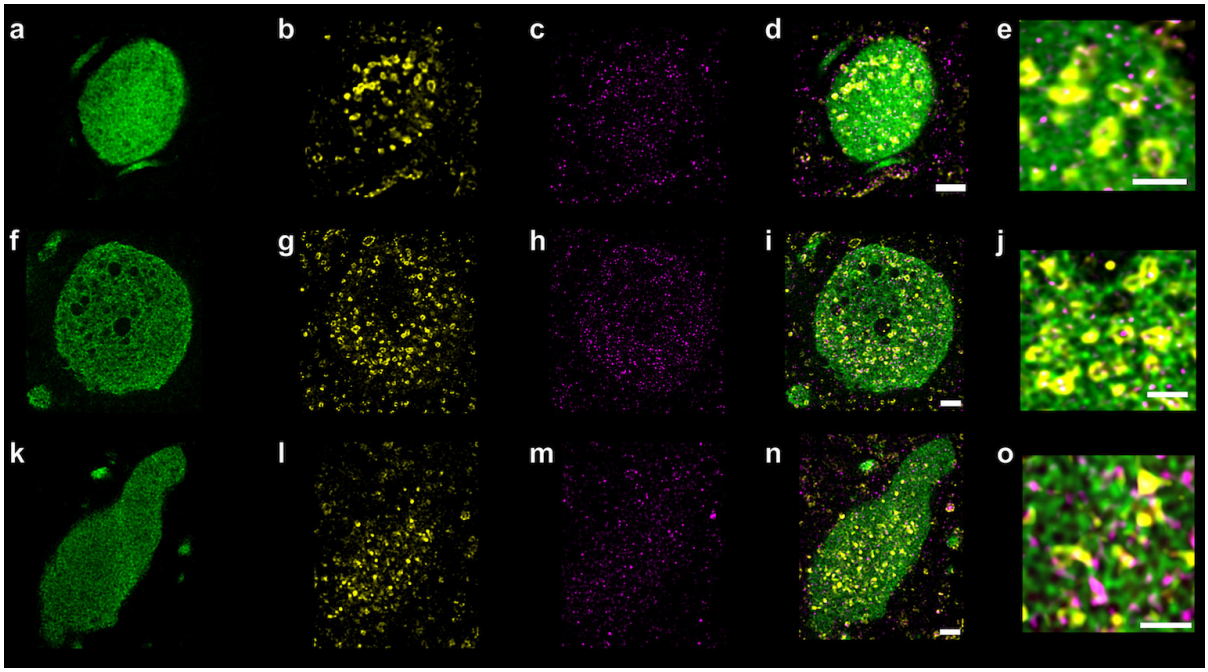

Figure S9. Subcellular distribution of aSyn and organelle markers within hippocampal Lewy bodies and Lewy neurites revealed by multi-labeling STED microscopy. STED microscopy showing distribution of (**a**) marker for phosphorylated aSyn (pS129), (**b**) marker for mitochondria (porin VDAC1), (**c**) marker for lysosomes (LAMP1), (**d**) overlay of 'a-c', (**e**) higher magnification view of the edge of the LB shown in 'd' (**f-i**) Same STED microscopy and markers as in 'a-d', but a different LB, (**j**) higher magnification view of center of the LB shown in 'i'. (**k-n**) Same STED microscopy and markers as in 'a-d,' but a LN, (**o**) higher magnification view of the LN as in 'n.'. Scale bars: d, i, n = 2 µm; e, j, o = 1 µm.

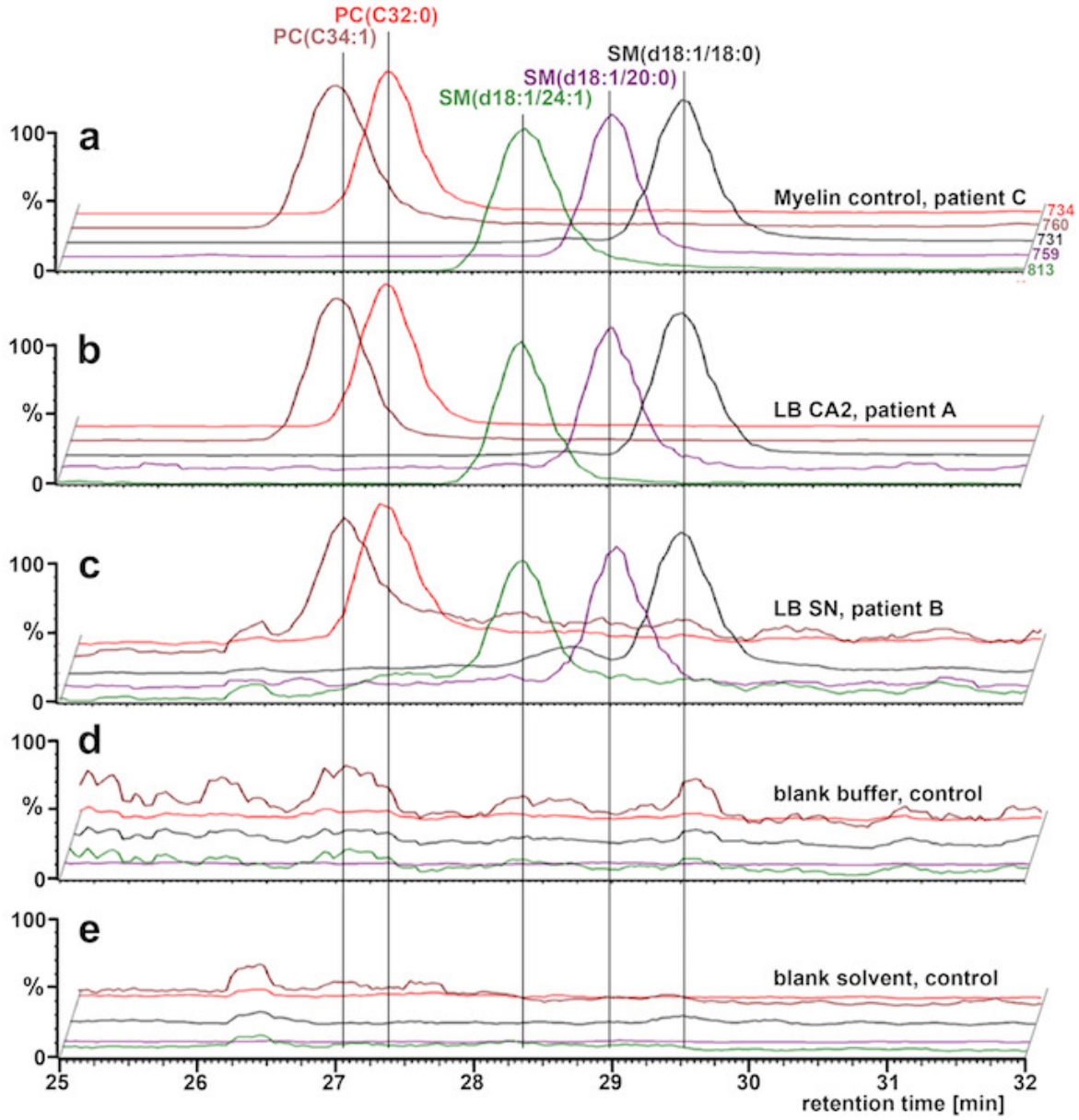

Figure S10. Liquid chromatography (LC) mass spectrometry (MS) and lipidomics reveal lipid content of Lewy bodies. Predominant peaks in all traces (**a–c**) represent the presence of phosphatidylcholine (PC) and sphingomyelin (SM) lipids. Mass spectrometric trace of (**a**) myelin as dissected from corpus callosum of non-demented control, Patient C, (**b**) laser capture micro-dissected LB (~2700) from hippocampal CA2 region of Patient A, (**c**) laser capture micro-dissected LB (~3050) from *substantia nigra* of Patient B. (**d**) Mass spectrometric traces of blank tube, and (**e**) blank solvent, 5 µl chloroform/MeOH (2:1), as control experiments. Each curve shows MS signal over LC retention time with the m/z window scanning for the ratios indicated at the right end of the curves in 'a'. These m/z windows select for the lipids indicated above the vertical lines in 'a'.

Movies

Movie 1: Reconstructed and color-segmented 3D transmission electron tomogram of Lewy body ("LB1"). Thickness of tissue section imaged ≈ 150 nm.

Movie 2: Reconstructed and color-segmented 3D transmission electron tomogram of Lewy body ("LB2"). Thickness of tissue section imaged ≈ 150 nm.

Movie 3: Reconstructed and color-segmented 3D transmission electron tomogram of a region inside Lewy body ("LB1") collected at higher magnification. The projection for this tomogram is not shown in Fig. 1 for reason of space. Thickness of tissue section imaged ≈ 150 nm.

Movie 4: Reconstructed and color-segmented 3D transmission electron tomogram of a region inside Lewy body ("LB1") collected at higher magnification. Tailed membrane stacks are clearly visible, as indicated in Fig. 1A (two yellow arrow-heads on right-hand side). Thickness of tissue section imaged ≈ 150 nm.

Movie 5: Reconstructed and color-segmented 3D transmission electron tomogram of region at the edge of the Lewy body ("LB1") collected at higher magnification. A mitochondrion is clearly visible, as indicated in Fig. 1i (white oval). Thickness of tissue section imaged ≈ 150 nm.

Movie 6: Reconstructed and color-segmented 3D transmission electron tomogram of region at the edge of the Lewy body ("LB2") collected at higher magnification. The projection for this tomogram is not shown in Fig. 1 for reason of space. Thickness of tissue section imaged ≈ 150 nm.

Movie 7: Reconstructed and color-segmented 3D transmission electron tomogram of region inside the Lewy body ("LB2") collected at higher magnification. Cluster of vesicles in separate adjacent compartment to LB2 is visible as shown in Fig. 1k. Thickness of tissue section imaged ≈ 150 nm.

Movie 8: Reconstructed and color-segmented 3D transmission electron tomogram of region within a Lewy neurite (same as shown in Fig. 2a) collected at high magnification. Thickness of tissue section imaged ≈ 150 nm.

Movie 9: Reconstructed and color-segmented 3D transmission electron tomogram of region within a Lewy neurite (same as shown in Fig. 2b) collected at high magnification. Thickness of tissue section imaged ≈ 150 nm.

Movie 10: Reconstructed and color-segmented 3D transmission electron tomogram of region within a 'control' neurite in brain tissue from a non-demented, age-matched donor (same as shown in Fig. 2c) collected at high magnification. Thickness of tissue section imaged ≈ 150 nm.

Movie 11: Reconstructed and color-segmented 3D transmission electron tomogram of region within a 'control' neurite in brain tissue from a non-demented, age-matched donor (same as

shown in Fig. 2d) collected at high magnification. Thickness of tissue section imaged ≈ 150 nm.

Movie 12: Reconstructed serial block-face scanning electron tomograms depicting three separate LB within the *substantia nigra* of Patient B. Scale bar = 5 µm.

Movie 13: Stimulated emission depletion microscopy showing a LB in the same tissues (Patient B, *substantia nigra*) as taken from parallel blocks for the SBFSEM ultrastructural analysis (Fig. 3d). Thickness of tissue section = 20 µm.

References

1. Goedert, M., Spillantini, M.G., Del Tredici, K. & Braak, H. 100 years of Lewy pathology. *Nat Rev Neurol* **9**, 13-24 (2013).
2. Wakabayashi, K., *et al.* The Lewy body in Parkinson's disease and related neurodegenerative disorders. *Mol Neurobiol* **47**, 495-508 (2013).
3. Arima, K., *et al.* Immunoelectron-microscopic demonstration of NACP/alpha-synuclein-epitopes on the filamentous component of Lewy bodies in Parkinson's disease and in dementia with Lewy bodies. *Brain Res* **808**, 93-100 (1998).
4. Klein, C. & Schlossmacher, M.G. Parkinson disease, 10 years after its genetic revolution: multiple clues to a complex disorder. *Neurology* **69**, 2093-2104 (2007).
5. Spillantini, M.G., *et al.* Alpha-synuclein in Lewy bodies. *Nature* **388**, 839-840 (1997).
6. Braak, H., Sandmann-Keil, D., Gai, W. & Braak, E. Extensive axonal Lewy neurites in Parkinson's disease: a novel pathological feature revealed by alpha-synuclein immunocytochemistry. *Neurosci Lett* **265**, 67-69 (1999).
7. Braak, H., Ghebremedhin, E., Rub, U., Bratzke, H. & Del Tredici, K. Stages in the development of Parkinson's disease-related pathology. *Cell Tissue Res* **318**, 121-134 (2004).
8. Lashuel, H.A., Overk, C.R., Oueslati, A. & Masliah, E. The many faces of alpha-synuclein: from structure and toxicity to therapeutic target. *Nat Rev Neurosci* **14**, 38-48 (2013).
9. Spillantini, M.G., Crowther, R.A., Jakes, R., Hasegawa, M. & Goedert, M. alpha-Synuclein in filamentous inclusions of Lewy bodies from Parkinson's disease and dementia with lewy bodies. *Proc Natl Acad Sci U S A* **95**, 6469-6473 (1998).
10. Forno, L.S. Neuropathology of Parkinson's disease. *J Neuropathol Exp Neurol* **55**, 259-272 (1996).
11. Hunn, B.H., Cragg, S.J., Bolam, J.P., Spillantini, M.G. & Wade-Martins, R. Impaired intracellular trafficking defines early Parkinson's disease. *Trends Neurosci* **38**, 178-188 (2015).
12. Morell, P.Q., R.H. The Myelin Sheath. in *Basic Neurochemistry: Molecular, Cellular and Medical Aspects. 6th edition.* (ed. A.B. Siegel GJ, Albers RW, et al., editors.) (Lippincott-Raven, Philadelphia, 1999).
13. Nixon, R.A. Autophagy, amyloidogenesis and Alzheimer disease. *J Cell Sci* **120**, 4081-4091 (2007).
14. Eichmann, C., *et al.* Preparation and Characterization of Stable alpha-Synuclein Lipoprotein Particles. *J Biol Chem* **291**, 8516-8527 (2016).
15. Liu, Y.L., *et al.* Alternation of neurofilaments in immune-mediated injury of spinal cord motor neurons. *Spinal Cord* **47**, 166-170 (2009).
16. Denk, W. & Horstmann, H. Serial block-face scanning electron microscopy to reconstruct three-dimensional tissue nanostructure. *PLoS Biol* **2**, e329 (2004).

17. Schie, I.W., Krafft, C. & Popp, J. Applications of coherent Raman scattering microscopies to clinical and biological studies. *Analyst* **140**, 3897-3909 (2015).
18. Baker, M.J., *et al.* Using Fourier transform IR spectroscopy to analyze biological materials. *Nat Protoc* **9**, 1771-1791 (2014).
19. Gai, W.P., *et al.* In situ and in vitro study of colocalization and segregation of alpha-synuclein, ubiquitin, and lipids in Lewy bodies. *Exp Neurol* **166**, 324-333 (2000).
20. Bras, J., Guerreiro, R. & Hardy, J. SnapShot: Genetics of Parkinson's disease. *Cell* **160**, 570-570 e571 (2015).
21. Hernandez, D.G., Reed, X. & Singleton, A.B. Genetics in Parkinson disease: Mendelian versus non-Mendelian inheritance. *J Neurochem* **139 Suppl 1**, 59-74 (2016).
22. Ryan, B.J., Hoek, S., Fon, E.A. & Wade-Martins, R. Mitochondrial dysfunction and mitophagy in Parkinson's: from familial to sporadic disease. *Trends Biochem Sci* **40**, 200-210 (2015).
23. Fernandes, H.J., *et al.* ER Stress and Autophagic Perturbations Lead to Elevated Extracellular alpha-Synuclein in GBA-N370S Parkinson's iPSC-Derived Dopamine Neurons. *Stem Cell Reports* **6**, 342-356 (2016).
24. Bingol, B., *et al.* The mitochondrial deubiquitinase USP30 opposes parkin-mediated mitophagy. *Nature* **510**, 370-375 (2014).
25. Wong, Y.C. & Krainc, D. alpha-synuclein toxicity in neurodegeneration: mechanism and therapeutic strategies. *Nat Med* **23**, 1-13 (2017).
26. Giasson, B.I., *et al.* Oxidative damage linked to neurodegeneration by selective alpha-synuclein nitration in synucleinopathy lesions. *Science* **290**, 985-989 (2000).
27. Gardiner, J., Overall, R. & Marc, J. The Nervous System Cytoskeleton under Oxidative Stress. *Diseases* **1**, 36-50 (2013).
28. Clague, M.J. & Rochin, L. Parkinson's Disease: A Traffic Jam? *Curr Biol* **26**, R332-334 (2016).
29. Burre, J. The Synaptic Function of alpha-Synuclein. *J Parkinsons Dis* **5**, 699-713 (2015).
30. Mizuno, N., *et al.* Remodeling of lipid vesicles into cylindrical micelles by alpha-synuclein in an extended alpha-helical conformation. *J Biol Chem* **287**, 29301-29311 (2012).
31. Dettmer, U., *et al.* Parkinson-causing alpha-synuclein missense mutations shift native tetramers to monomers as a mechanism for disease initiation. *Nat Commun* **6**, 7314 (2015).
32. Altmeyer, M., *et al.* Liquid demixing of intrinsically disordered proteins is seeded by poly(ADP-ribose). *Nat Commun* **6**, 8088 (2015).
33. Emre, M., *et al.* Clinical diagnostic criteria for dementia associated with Parkinson's disease. *Mov Disord* **22**, 1689-1707; quiz 1837 (2007).

34. Braak, H., Alafuzoff, I., Arzberger, T., Kretzschmar, H. & Del Tredici, K. Staging of Alzheimer disease-associated neurofibrillary pathology using paraffin sections and immunocytochemistry. *Acta Neuropathol* **112**, 389-404 (2006).

35. Thal, D.R., Capetillo-Zarate, E., Del Tredici, K. & Braak, H. The development of amyloid beta protein deposits in the aged brain. *Sci Aging Knowledge Environ* **2006**, re1 (2006).

36. McKeith, I.G.*, et al.* Diagnosis and management of dementia with Lewy bodies: third report of the DLB Consortium. *Neurology* **65**, 1863-1872 (2005).

37. Mastronarde, D. SerialEM A program for automated tilt series acquisition on tecnai microcopes using prediction of specimen position. *Micros Microanal* **9**, 1182-1183 (2003).

38. Hagen, W.J., Wan, W. & Briggs, J.A. Implementation of a cryo-electron tomography tilt-scheme optimized for high resolution subtomogram averaging. *J Struct Biol* (2016).

39. Kremer, J.R., Mastronarde, D.N. & McIntosh, J.R. Computer visualization of three-dimensional image data using IMOD. *J Struct Biol* **116**, 71-76 (1996).

40. Castano-Diez, D., Kudryashev, M., Arheit, M. & Stahlberg, H. Dynamo: a flexible, user-friendly development tool for subtomogram averaging of cryo-EM data in high-performance computing environments. *J Struct Biol* **178**, 139-151 (2012).

41. Ivanova, P.T., Milne, S.B., Byrne, M.O., Xiang, Y. & Brown, H.A. Glycerophospholipid identification and quantitation by electrospray ionization mass spectrometry. *Methods Enzymol* **432**, 21-57 (2007).

42. El-Mashtoly, S.F.*, et al.* Automated identification of subcellular organelles by coherent anti-stokes Raman scattering. *Biophys J* **106**, 1910-1920 (2014).

43. Wrobel, T.P., Wajnchold, B., Byrne, H.J. & Baranska, M. Electric field standing wave effects in FT-IR transflection spectra of biological tissue sections: Simulated models of experimental variability. *Vibrat Spectr* **69**, 84-92 (2013).

44. Kallenbach-Thieltges, A.*, et al.* Immunohistochemistry, histopathology and infrared spectral histopathology of colon cancer tissue sections. *J Biophotonics* **6**, 88-100 (2013).

45. Bassan, P.*, et al.* FTIR microscopy of biological cells and tissue: data analysis using resonant Mie scattering (RMieS) EMSC algorithm. *Analyst* **137**, 1370-1377 (2012).

46. Ellisman, M.H., Deerinck, T.J., Shu, X. & Sosinsky, G.E. Picking faces out of a crowd: genetic labels for identification of proteins in correlated light and electron microscopy imaging. *Methods Cell Biol* **111**, 139-155 (2012).

47. Förstl, H.H., Martin; Roth, Gerhard. *Neurobiologie psychischer Störungen* (Springer-Verlag Berlin Heidelberg, 2006).